

Computational Studies on Structure and Mechanical Properties of Carbides in
HCCIs

by

Juan Cui

A thesis submitted in partial fulfillment of the requirements for the degree of

Master of Science

in

Materials Engineering

Department of Chemical and Materials Engineering
University of Alberta

© Juan Cui, 2017

Abstract

High Chromium Cast Irons (HCCIs) are widely used in mineral processing, slurry pumping and manufacturing processes, where high resistance to erosion and synergetic erosion-corrosion is required. The excellent performance of HCCIs results from their microstructure, which consists of hard carbides (mainly in hypereutectic HCCI) and ferrous matrix (austenite or martensite). The matrix helps absorb impact force and enhance toughness of the material, while the hard carbides play a crucial role in withstanding the wearing stress. Due to different processing treatments and chemical compositions, the morphology and mechanical properties of carbides can vary significantly, which affects HCCIs' wear performance.

In this study, the effect of core-shell structured carbides on HCCIs' wear performance and the effect of Cr content on M_7C_3 carbides' mechanical properties are studied by different simulation methods. C++ programming based MSDM method is used to study and optimize the core-shell structured carbides, which have been proved beneficial to HCCIs' wear resistance. By measuring local properties, including Young's modulus and electron work functions, and conducting first-principles calculations for individual phases, HCCIs' erosion-corrosion

performance in slurry are better understood. At last, the correlation between Young's modulus and electron work function is explained by first-principles calculation from an electronic view.

Preface

Results presented in Chapter 3 of this thesis have been published in *Tribology International*: Cui, Juan, et al., A computational study on the benefit of core-shell structured carbides to the erosion resistance of high-Cr cast irons *Tribology International*, 103 (2016): 432-439.

Results presented in Chapter 4 of this thesis have been accepted by *Wear*: Juan Cui, Liqiu Guo, Hao Lu, D.Y. Li, Understanding effects of Cr content on the slurry erosion behavior of high-Cr cast irons through local property mapping and computational analysis, *Wear* (2017).

For the above publications, I am responsible for computational studies, including MSDM modeling, first-principles calculations, data analysis, investigation of underlying mechanisms, and composing manuscripts. I have also been involved in experiments for hardness measurements and participated in collaboration with colleagues and industrial partners as mentioned below.

Dr. Hong Guo performed FEM analysis reported in Chapter 3; Dr. Liqiu Guo performed measurement of work function with AFM shown in Chapters 4 and 5. The data of slurry erosion tests and SEM/EDX results are contributed by Dr. Reinaldo and Dr. X. H. Tang, respectively. Hao Lu, Dr. J. W. Li, Leo Parent and Dr. Harry Tian participated in data analysis and discussion for the first publication. Hao Lu also assisted hardness test and data analysis for the second publication. Professor D.Y. Li contributed to data analysis and manuscripts revisions. All the investigations

are conducted under Professor D.Y. Li's supervision.

Acknowledgement

First of all, I want to thank my supervisor, Dr. Dongyang Li, who gave me patient guidance, a great deal of encouragement and valuable suggestions during my whole graduate study.

I also want to thank the committee members, who made comments and suggestions on my thesis.

My special thanks are due to Dr. Ziran Liu, Dr. Hong Guo, Dr. Liqui Guo and all my group members, from whom I learned a lot of skills in computational study and experiments.

I would also like to thank my parents and husband for their support.

Computational resources provided by WestGrid and Financial support from Natural Science and Engineering Research Council of Canada (NSERC), Suncor Energy Inc. and GIW Industries are gratefully appreciated.

Table of Contents

1 Introduction and Literature Review	1
1.1 Influence of Cr content on HCCI's properties.....	1
1.2 Core-shell structured carbides.....	2
1.2.1 Formation of core-shell structured carbides.....	2
1.2.2 Morphology of core-shell structured carbides	3
1.2.3 Benefits of core-shell structured carbides	4
1.3 Object of this study	7
2 Simulation methods.....	9
2.1 Micro-Scale Dynamic Model (MSDM) - a model for wear simulation.....	9
2.2 First-Principles Calculation.....	14
2.2.1 Description of First-Principles Calculation.....	14
2.2.1.1 Approximation of Schrödinger equation.....	15
2.2.1.2 Energy Operator: Hamiltonian.....	16
2.2.1.3 Many electron problem	16
2.2.1.4 Variational principle to search for ground state	18
2.2.2. Density Functional Theory.....	18
2.2.2.1 Hohenberg-Kohn Theorem	18
2.2.2.2 Kohn-Sham Equation.....	19
2.2.2.3 Exchange-Correlation (XC) functionals	20
2.2.2.4 Iterative variational approach.....	21
2.2.3 Pseudopotentials (PPs).....	22

3 A Microscale Dynamic Model for Wear Simulation of Core-shell Structured High Cr Cast Irons	23
3.1 The modeling procedure	23
3.2 Stress/strain analysis using FEM	27
3.3. Results and discussion.....	28
3.3.1 Effects of the core-shell structured carbides on erosion of HCCIs.....	28
3.3.1.1 Solid particle erosion and the performance of the core-shell carbide	28
3.3.1.2 Influence of the shell thickness on erosion	30
3.3.1.3 Influences of carbide shape and orientation on erosion.....	31
3.3.2.2 Influence of the carbide orientation on stress distribution.....	35
3.3.2.3 Influence of the shell thickness	37
3.4 Summary	38
4 Understanding Effects of Cr content on the Slurry Erosion behavior of High-Cr cast irons through Local property mapping and Computational analysis	40
4.1 Experiment Details.....	41
4.1.1 Sample Preparation	41
4.1.2 Slurry erosion testing	42
4.2 Computation details	44
4.3 Results and discussion.....	45
4.3.1 Microstructure	45
4.3.3. Work function, modulus and hardness of Fe _{7-x} Cr _x C ₃ and matrix.....	51

4.4 First-Principles Calculation.....	54
4.4.1 Mechanical properties of carbides	54
4.4.2 Potential and charge density of the ferrous matrix.....	56
4.5 Understand of the overall performance.....	57
4.6 Summary	58
5 Further studies on the correlation between electronic and mechanical properties of (Fe, Cr)₇C₃ carbides.....	60
5.1 Carbides Young's modulus VS Electron work function.....	60
5.2 Results and discussion.....	61
5.2.1 Structure and formation energy.....	61
5.2.2 Density of states (DOS) and Bader charge analysis.....	62
5.2.3 Electron density (e/angstrom ³)	65
5.2.4 Further discussion on mechanism	66
5.3 Summary	67
6 General Conclusions and Future Work	69
6.1 General conclusions of the research.....	69
6.2 Future work	70
6.2.1 Extend MSDM to 3-dimensional calculation.....	70
6.2.2 Interfacial bonding strength	70

List of Tables

Table 3.1 Mechanical properties of the modeled materials [11].....	25
Table 4.1 Measured average values of compositions and Cr/Fe ratios of (Fe, Cr) ₇ C ₃ carbide and matrix in the HCCIs determined with EDX.	47
Table 5.1 Calculated coordinates of atoms and formation energy of (Fe, Cr) ₇ C ₃ . ..	62
Table 5.2 Bader charge transfers from metal to carbon atoms (e/atom). Values positive mean lose electron and negative mean get electron.	64

List of Figures

Figure 1.1 Back-scattered electron images of HCCI with 45 wt.% Cr and 4 wt.% C [7].	4
Figure 1.2 (a) Bulk hardness of HCCI 45-series; (b) Morphologies of dents on HCCI 45-series; (c) Resistance of 45-4 to abrasive wear (red line) under the condition of procedure A of ASTM G65 rubber-wheel abrasion testing and slurry-pot erosion (blue line) in silica sand-containing tap water at pH3 cited from [11].	7
Figure 2.1 Schematic illustration of a linear approximation of stress–strain curve [20].	11
Figure 2.2 Schematic of a typical DFT procedure by iterative self-consistent loop [27].	21
Figure 3.1 A model system used for simulation. The core-shell hexagon represents the M_7C_3 core (green) surrounded by $M_{23}C_6$ shell (red). $R_1=14\mu\text{m}$, $R_2=20\mu\text{m}$; The thickness ratio of core to shell is about 2.3:1. The yellow square represents an ejected erodent particle. The shape of the carbide can be modified for more general situations.	23
Figure 3.2 A cross-sectional view of a FEM model for analyzing stress/strain distribution around a core-shell carbide in comparison with a single-phase carbide (i.e. shell thickness = zero).	28
Figure 3.3 A. (a) A system consisting of iron and M_7C_3 layers struck by a spherical solid particle at an angle of 45° with a velocity of 4.0m/s, and (b) a system consisting of iron, $M_{23}C_6$ and M_7C_3 layers under the same striking condition. B.	

Material losses caused by erosion (modeling and experimental).....	30
Figure 3.4 A - Influence of the shell thickness on erosion; B - Corresponding configurational changes caused by erosion of HCCI samples containing core-shell carbides with different shell thickness values: (a) 0 um, (b) 6 um, (c) 8um, and (d) 10 um. The impingement angle is 45°.	31
Figure 3.5 A - Five carbide configurations were used to investigate influences of carbide shape and orientation on wear loss; Impingement angle = 45° and the ratio of length to width of carbide, i.e. a/b ratio, are (a) 3, (b) 2, (c) 1, (d) 1/2 and (e) 1/3. B - Site losses of the five model systems under the same erosion condition.	33
Figure 3.6 (a) Isolines of principal stress around a M_7C_3 carbide, (b) isolines of shear stress around the M_7C_3 carbide; (c) isolines of principal stress around a core-shell carbide, and (d) isolines of shear stress around the core-shell carbide. ..	35
Figure 3.7 Isolines of principal stress for vertically and horizontally aligned carbides.	36
Figure 3.8 Schematic illustration of two possible situations: (a) the horizontally lied carbide could suffer from bending and interfacial debonding, thus likely triggering global failure; (b) the vertically lied one may suffer more from local damage but has a lower probability for cracking spreading.	37
Figure 3.9 Variations in maximum principal and shear stresses with respect to the shell thickness. (a) Vertically aligned carbide; (b)Horizontally aligned carbide.	38
Figure 4.1 Back-scattered electron (BSE) micrographs of microstructures of (a) #5-5, (b) #10-5, (c) #20-5, (d) #30-5, (e) #35-5.	46
Figure 4.2 Weight-loss mapping of varied chromium iron dependent of chromium concentration at 45°impinging angle in pH=5(a) and pH=3(b), respectively. During	

the slurry erosion test, a sample travelled over 15 km.	49
Figure 4.3 (a) A MFM image of a #20-5 HCCI, (b) corresponding work function map, and (c) corresponding modulus map (zones in green have higher modulus)..	52
Figure 4.4 The experimentally measured (a) modulus and (b) work function (c) microhardness of carbides and matrix and (d) Macro-hardness of samples at different Cr content levels.	53
Figure 4.5 (a) Bulk modulus(B), shear modulus(G) and Young's modulus(E) of samples; (b) The hardness Hv calculated by Eq. (4.1).	56
Figure 4.6 (a) a BCC structured 15Fe (golden)-1Cr (blue) alloy cell, (b) a local potential plot of (110) plane, and (c) an electron density plot of (110) plane.	57
Figure 5.1 Measured work function and Young's modulus of carbides in samples #5-5, #10-5, #20-5 and #35-5.	60
Figure 5.2 (a) Atomic structure of M_7C_3 carbide. (large: metal; small: carbon) (b) (110) plane configuration of M_7C_3 carbide. (purple: metal; grey: carbon)	61
Figure 5.3 Atom-projected densities of states for bulk $Fe_{7-x}Cr_xC_3$ carbide systems. For each system, band overlap of metal and carbon near -5eV are responsible for covalent bond between metal-carbon.	63
Figure 5.4 Electron density distribution of the (110) plane of Fe_7C_3 (a), $Fe_6Cr_1C_3$ (b), $Fe_4Cr_3C_3$ (c), $Fe_3Cr_4C_3$ (d), $Fe_1Cr_6C_3$ (e) and Cr_7C_3 (f). For each system, minimum, maximum and isoline values are set the same. Electron densities between metal-metal atoms are most pronounced in c) and d), and are responsible for their high Young's modulus.	65

List of Abbreviations

2D	Two dimensional
3D	Three dimensional
AFM	Atomic force microscopy
B	Bulk modulus
BSE	Back-scattered electron
DFT	Density functional theory
DOS	Density of states
E	Young's modulus
EBSD	Electron backscatter diffraction
EDX	Energy dispersive X-ray analysis
EFW	Electron work function
FEM	Finite element method
G	Shear modulus
GGA	Generalized gradient approximation
HCCI	High Cr cast iron
KPFM	Kelvin probe force microscope
LDA	Local density approximation
MD	Molecular dynamics
MFM	Magnetic force microscopy
MSDM	Micro-scale dynamic method
PAW	Projector-augmented wave
PP	Pseudopotential
SEM	Scanning electron microscope
TEM	Transmission electron microscope
USPP	Ultrasoft pseudopotential
XC	Exchange-correlation
XRD	X-ray diffraction
ΔH	Formation enthalpy

1 Introduction and Literature Review

1.1 Influence of Cr content on HCCI's properties

Although HCCIs are iron-based alloys, their compositions of Cr and C are crucial, since they are essential to the material for forming carbides. Content of carbon is directly responsible for the formation of carbides in microstructure. As carbon content increases, the volume fraction of carbides increases, which would enhance HCCIs' hardness and wear resistance. However, such improvement is at the expense of fracture toughness and hardenability. Too much carbon would make the sample brittle, which is undesired in industry.

Chromium is easier than iron to form carbides since the formation energy decreases as chromium is added [1]. Chromium helps form carbides in a ferrous matrix and prevents the formation of graphite, thus enhancing hardness of the material [2]. Commercially used chromium cast irons are mainly in the state of hypoeutectic, with compositions in the range of 10-30 wt% Cr, 2-3.5 wt% C and other elements such as Mo, Ni, and Cu to add hardenability [3]. They are designed for anti-wear applications. Among them, alloys with 28-30 wt% Cr and 2-2.7 wt% C are developed to resist combined attacks of erosion and corrosion encountered in wet grinding and slurry transport processes [4]. Since corrosion mainly occurs in the matrix, the high concentration of Cr in the matrix leads to high corrosion resistance in such severe environments[5]. For oil sands industry in Alberta, HCCIs are

extensively used in slurry pumping and transportation.

Although it is known that adding both chromium and carbon can improve wear and corrosion resistance simultaneously, pushing Cr content to higher levels is not easy until recent years, with the advance in foundry techniques, which has made it possible to cast hypereutectic alloys with high carbon and chromium concentrations [6]. Such cast irons were previously considered to be non-castable due to high scrap and rejection rates. Recently, in Tang's research, HCCIs with chemical compositions of chromium (45 wt.%), silicon (0.5 wt.%), manganese (2 wt.%), and various concentrations of carbon: 1, 2, 3, 4, 5 and 6 wt.%, respectively, balanced by iron, were cast for erosion-corrosion tests. It is demonstrated that hypereutectic alloys have much higher volume fractions of hard carbides and less volume loss than hypoeutectic alloys during erosion-corrosion tests [7].

1.2 Core-shell structured carbides

1.2.1 Formation of core-shell structured carbides

The as-cast alloys with 28-30 wt.% Cr and 2-2.7 wt.% C contain M_7C_3 -type eutectic carbides in a matrix of austenite with partial transformation of the austenite to martensite in eutectic regions [4]. Since austenite is not hard enough (500-520HV), in most cases, heat treatment is needed. Conventional heat treatment involves heating castings to and holding at 950–1050°C for 1-4h, followed by air cooling and tempering. The holding period is called “destabilization” [8]. The primary purpose of heat treatment is to lower the alloy content of the austenite by precipitation of

secondary carbides in matrix and enable the austenite to transform to martensite on forced air-cooling. The purpose of tempering after destabilization at 450-650 °C for normally 4 hours is to reduce the amount of the retained austenite in the matrix and the residual stress after quenching. The resultant microstructure consists of eutectic carbide (M_7C_3) and secondary carbides distributed in a martensite matrix with small amount of retained austenite. The hardness levels are increased to about 700-850 HV and thus erosive wear resistance are enhanced [3].

Destabilization treatments do not appear to have any significant effects on the formation of the eutectic carbides in irons containing up to about 28% Cr. However at the 30% Cr, destabilization treatments cause M_7C_3 carbide to partially transform to $M_{23}C_6$ carbide [8]. Under TEM examination, this $M_{23}C_6$ carbide can be recognized as shells surrounding the M_7C_3 cores [9]. Such core-shell structured carbides could also be found in primary carbides of hypereutectic HCCIs with higher chromium contents. For example, Tang's 45-4 sample confirmed such core-shell structured primary carbides [7]. The present findings believe that $M_{23}C_6$ nucleate at the original interface between M_7C_3 carbides and the matrix and then grows inwards consuming M_7C_3 carbides [4].

1.2.2 Morphology of core-shell structured carbides

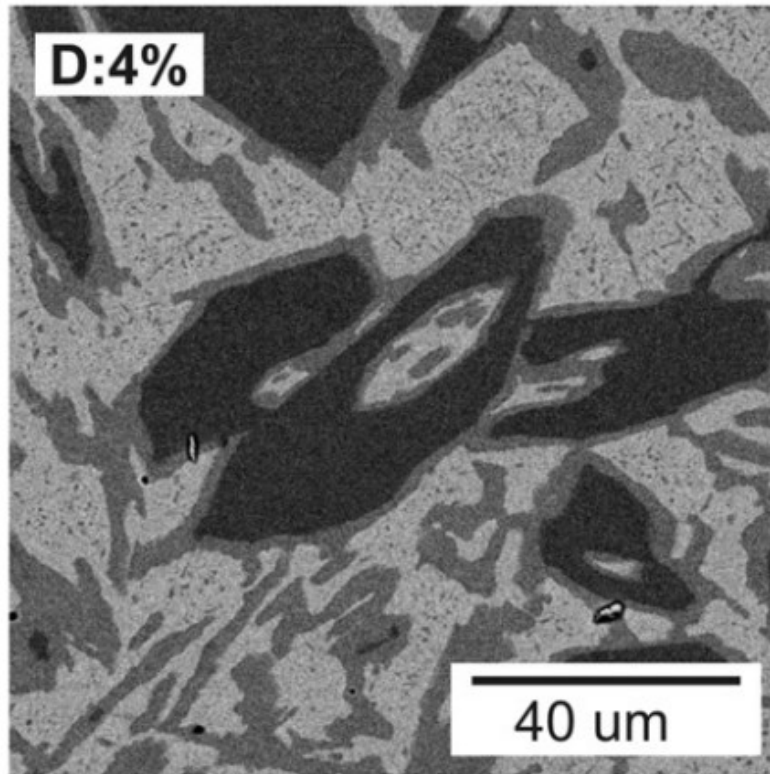
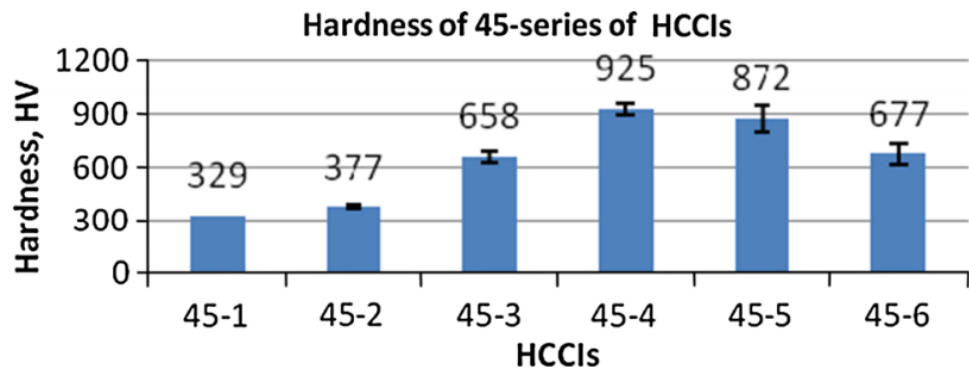


Figure 1.1 Back-scattered electron images of HCCI with 45 wt.% Cr and 4 wt.% C [7].

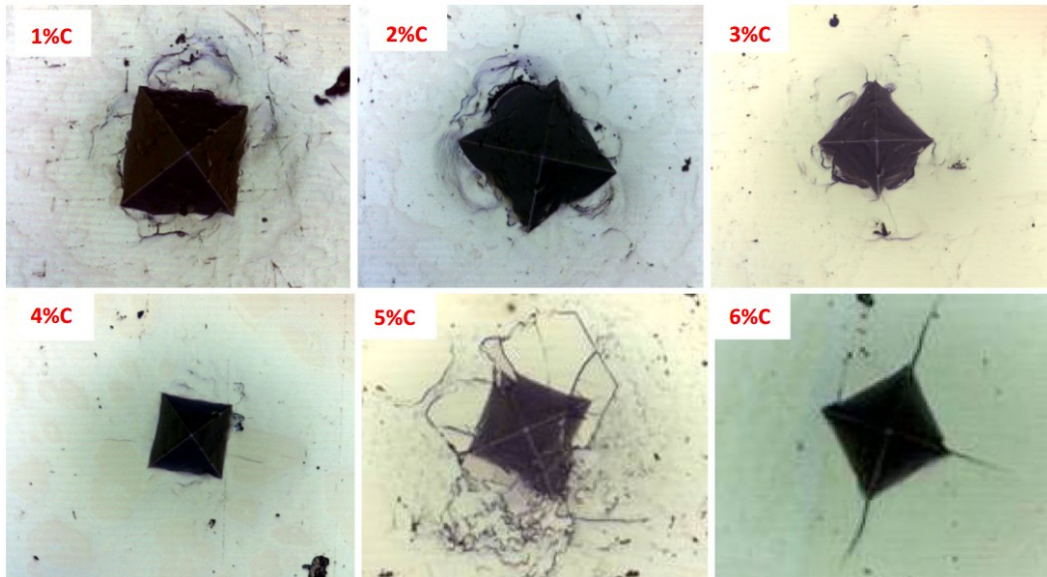
Fig 1.1 shows the microstructure of Tang's 45-4 sample, which consists of matrix of martensite, rod-like primary carbides with a hexagonal cross-section and fine eutectic carbides. The primary carbides have a duplex structure showing a dark core surrounded by a lighter layer or shell, as shown in Fig. 1.1. According to combined analysis of EDX, XRD and EBSD, the core and the lighter shell are identified as M_7C_3 and $M_{23}C_6$ respectively [7]. The shell thickness can be controlled by destabilization time [9].

1.2.3 Benefits of core-shell structured carbides

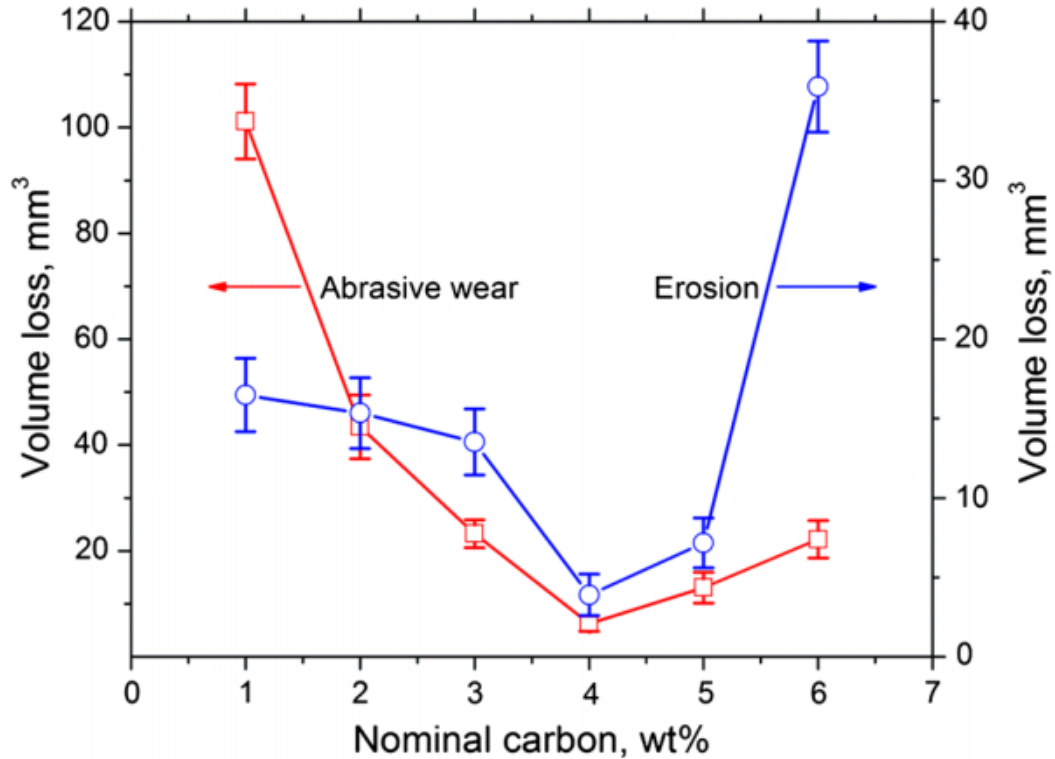
Increasing the content of Cr, a strong carbide-forming element, helps increase hardness of HCCIs but this however deteriorates their fracture toughness. Commercially used HCCIs have their chromium content in the range of 23-30 wt.% Cr, in which the core-shell structured carbides may not form or just form as eutectic carbides, rather than primary carbides since they have hypoeutectic microstructure. In the case of HCCIs with core-shell structured eutectic carbides, lack of improvement for both dry and wet wear resistance after destabilization treatments was observed and it was believed that the reason is the $M_7C_3 \rightarrow M_{23}C_6$ transformation in the eutectic carbides, that have a greater tendency to crack and become detached during wear [8, 10]. However, in hypereutectic HCCIs with higher Cr content level, the formation of core-shell structured primary carbides has been experimentally demonstrated to be beneficial to the wear resistance of HCCIs, largely attributed to reduced stress concentration at carbide/matrix interface [7, 11]. This helps improve the toughness of HCCIs through minimizing the risk of interfacial failure, making it achievable to develop HCCIs with higher toughness while retaining desired hardness that high Cr content brings. Thus, it would be applicable for more severe conditions involving large wearing stress and impact. Tang *et al* investigated HCCIs with 45wt.%Cr, called 45-series, and demonstrated that HCCI 45-4 with 4wt.%C, in which core-shell structured carbides were observed, performed the best among 45-series during abrasion and erosion tests [7, 11], as shown in Fig. 1.2. The shell is softer but tougher than the core. Static stress analysis showed that the shell had its hardness between those of the harder core and soft ferrous matrix, which helped reduce the interfacial stress caused by the mismatch between the hard carbide and soft matrix [11].



(a)



(b)



(c)

Figure 1.2 (a) Bulk hardness of HCCI 45-series; (b) Morphologies of dents on HCCI 45-series; (c) Resistance of 45-4 to abrasive wear (red line) under the condition of procedure A of ASTM G65 rubber-wheel abrasion testing and slurry-pot erosion (blue line) in silica sand-containing tap water at pH3 cited from [11].

1.3 Object of this study

1. In order to obtain more information on the effect of core-shell structured carbides on wear and maximize their benefits, a micro-scale dynamic method (MSDM) was employed to investigate how the shell thickness and geometry of the carbide would

affect the erosion and impact resistance of the material. Stress/strain state of the core-shell structured carbides and their variations with the core-shell configuration were also analyzed with the finite element method (FEM) in order to better understand underlying mechanisms.

2. In the second study, in order to understand the effects of chromium content, in the range of 5~35%Cr, on the performance of HCCIs containing 5%C during erosion tests in slurries with two pH values and four velocities, local mechanical properties and electron work function, which is a measure of surface activity, were analyzed for both the ferrous matrix and $(\text{Fe, Cr})_7\text{C}_3$ carbides using a micro-indenter and a multi-mode atomic force microscope. First-principles calculation was conducted to analyze $(\text{Fe, Cr})_7\text{C}_3$ carbides and the matrix to understand mechanisms responsible for observed phenomena.

3. In order to illustrate the phenomena observed in previous study that the trend of $(\text{Fe, Cr})_7\text{C}_3$ carbides' mechanical properties is consistent with that of measured work functions. First-principles calculation of $(\text{Fe, Cr})_7\text{C}_3$ carbides with different Cr/Fe ratios was conducted for further understanding of the mechanism.

2 Simulation methods

2.1 Micro-Scale Dynamic Model (MSDM) - a model for wear simulation

Computational models proposed for wear simulation may be classified into two groups: macro-modeling and atomistic modeling. The former is proposed with existing tribological rules, empirical equations, assumptions or theories based on macro-mechanical properties [12] , e.g., the removal of material is determined by the critical plastic strain. The continuum mechanical models or those with empirical rules can be used to determine the severity of wear under specific wearing conditions and to predict service life of a system with known material properties. However, the wear resistance of a material is largely affected by its microstructure. The macro-modeling does not provide information for tribo-material modification through microstructure control. Thus, the macro-modeling is not used to predict material behavior but to determine the wearing condition for maintenance purpose, e.g., for estimating the service life of a pipeline subjected to erosion. Finite element method (FEM) is also used for wear simulation[13-15]. It divides the system into many small elements and calculates variables such as stress, strain, temperature, and pressure. Sets of equations are solved by a computer-based numerical technique. This method can provide information on the stress/strain distribution, which helps to predict the initiation of surface failure for the scale of real components. However, continuous changes in surface geometry during wear make it difficult to simulate

using FEM for an entire wear process. Nevertheless, efforts are continuously made to facilitate wear analysis using FEM, e.g., Wang [16] combined FEM and a meshfree method to analyze erosive wear, which saved computer time. Atomistic modeling developed based on fundamental physics laws is effective for simulating wear of materials, such as the molecular dynamics simulation[17] and the first-principle technique[18]. The atomistic modeling help understand local wearing events and material behavior. However, the limited capability of current computing facilities makes it difficult to simulate wear of materials involving microstructural effects, which requires handling a large number of atoms.

MSDM is a simple and flexible technique, which has been proven effective for modeling different wear processes for materials design or modification [19-21]. It is a micro-scale model and are used to track the position and trajectory of material clusters during simulated wear processes based on Newton's law of motion and basic mechanical properties. MSDM has been successfully applied in modeling abrasive, sliding and corrosive wear processes [22, 23]. In this study, stress/strain state of the core-shell structured carbide and its variations with the core-shell configuration were also analyzed with the finite element method (FEM) in order to better understand underlying mechanisms. For self-containing, a brief introduction to the MSDM method and main equations are provided here.

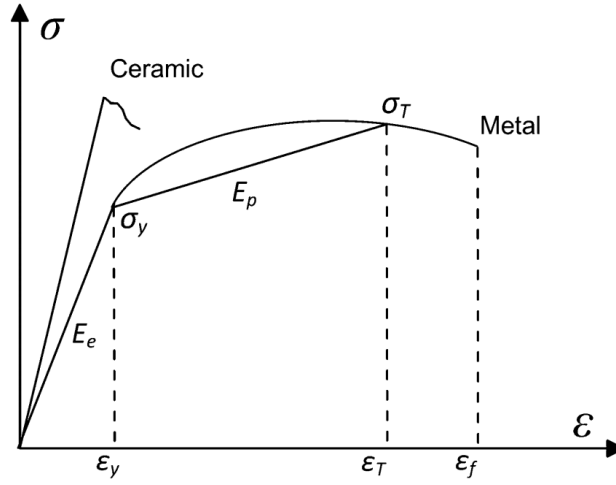


Figure 2.1 Schematic illustration of a linear approximation of stress–strain curve [20].

In this model, the erodent particle and the target material are discretized and mapped onto a 2D square lattices, respectively. Each lattice site represents a small volume of material. The strength of the bond between two sites is determined by mechanical properties of the materials involved, which can be measured experimentally. The movement of each lattice site is determined based on Newton's law of motion: $\vec{F} = m(d^2\vec{r}/dt^2)$, where \vec{r} is the position vector of the lattice site and m is the mass of the site. The force exerted on this site, \vec{F} , includes the internal interaction force from adjacent sites and the external force from the erodent impact if the site is on the surface and have direct interact with the erodent. The site-site interaction force is proportional to the deformation of the bond between the adjacent sites, which can be expressed as: $\vec{F} = k \cdot \Delta l \cdot \vec{n}$, where $\Delta l = l - l_0$ is the deformation of the bond between a pair of adjacent sites. l_0 is the length of bond in

stress-free condition and l is length of bond with deformation. It should be noticed is that the term 'bond' here is not referred to the atomic bond between atoms but one similar to a spring connecting two adjacent material clusters or sites having a small volume, and $k = E \cdot l_0$ is the force coefficient or spring constant, which characterizes the interaction between two sites. As shown in Fig. 2.1, when Δl is in the elastic region, E is the Young's modulus, $E = E_e = \frac{\sigma_y}{\varepsilon_y}$, where σ_y and ε_y are yield stress and yield strain. Once Δl exceeds the elastic region, a so-called plastic modulus, $E = E_p = \frac{(\sigma_T - \sigma_y)}{(\varepsilon_f - \varepsilon_y)}$ is used, where σ_T and ε_f are the tensile stress and fracture strain. E_p reflects the resistance to irreversible plastic deformation and also the strain hardening capability. For the bond between metal sites, it has both elastic and plastic modulus, while for the bond between ceramic sites, it only has an elastic modulus. For a site on the target material surface, an external force \vec{J}_p caused by particle impact needs to be taken into account. Thus, the total force exerted on a site denoted as p is expressed as:

$$\vec{F}_p = \sum_q n \cdot \Delta l(p, q) + \vec{J}_p \quad (2.1)$$

where p and q represent two adjacent sites, n is the number of sites adjacent to site p .

The interfacial bond between two different materials is considered to be the same as one of the materials but the join point is perfect since the scale of bonds in this

model is much larger than actual interfacial bonds between atoms. This assumption, though simplifies the situation of interfacial bonding, does not affect the conclusion drawn from the micro-scale stress analysis for the carbide/matrix interface. More accurate interfacial bonding analysis could be achieved using other methods, such as the first-principle method.

Then the velocity and the next position of site p after a time interval Δt may be determined by velocity Verlet algorithm,

$$\vec{v}_{t+\Delta t}(p) = \vec{v}_t(p) + \frac{\vec{F}_t(p)}{m} \cdot \Delta t \quad (2.2)$$

$$\vec{r}_{t+\Delta t}(p) = \vec{r}_t(p) + \frac{\Delta t}{2} [\vec{v}_t(p) + \vec{v}_{t+\Delta t}(p)] \quad (2.3)$$

where $\vec{v}_t(p)$ and $\vec{v}_{t+\Delta t}(p)$ are velocities of site p at time t and $t + \Delta t$, respectively. m is the mass of site p; $\vec{r}_t(p)$ and $\vec{r}_{t+\Delta t}(p)$ are position vectors at time t and $t + \Delta t$, respectively. A very small Δt can be used to capture more details during the dynamic process if simulation time is not an issue. However, in order to save computing time without missing necessary information, a reasonably small Δt would be sufficient, which can be determined through several trials to make it small enough with stable outcome. More discussion on Δt selection can be found in a reference[24]. By repeating the calculations, trajectory and velocity of each site can be determined. A bond is not broken under compression but breaks if it is elongated with its deformation exceeding the corresponding fracture strain. A site or a cluster

of sites is worn away during wear if all the bonds connecting to the site are broken. The volume loss is calculated based on the number of sites worn away according to the following equation:

$$\text{Volume loss} = \text{number of sites worn away} \times l_0^3 \quad (2.4)$$

More details have been described in previous publications [19-23, 25].

2.2 First-Principles Calculation

In molecular dynamic modeling (MD), atoms are as the basic particles, and nuclei and electron are disregarded. The origins of potentials, nuclei, and electrons are excluded and the interacting potential between atoms are empirically generated in this method. For this reason, electronic and magnetic properties cannot be analyzed. Unlike MD, the first-principles methods treat nuclei and electrons as the basic particles and describe events in a subatomic world. The system is expressed only by quantum mechanics that involves relatively difficult partial differential equations. Thus, first-principles calculations do not depend on any external parameters except the atomic numbers of the constituent atoms to be simulated. In the 1930s, only simple hydrogen-like atoms were calculated with quantum mechanical methods, but now the number of atoms has been increased to several thousands by the advent of density functional theory (DFT). All properties including electronic and magnetic can be obtained given that nuclei and electrons are considered in the method.

2.2.1 Description of First-Principles Calculation

The *Ab initio* method is based on theory from first-principles without including any empirical data. It usually uses the Born-Oppenheimer approximation [26], which greatly simplifies the Schrödinger equation and makes the calculation easier. Through searching for the minimum energy of the system, a stable system at ground state is obtained along with all energetic properties. Although these complicated theories and mathematics are embedded in software that we may not need to know, basic concepts are briefly introduced below to make it understandable. More details of first-principles calculation and density functional theory are available in book references [27, 28].

2.2.1.1 Approximation of Schrödinger equation

Schrödinger equation [29] describes how the quantum state of a physical system changes in time.

$$H\Psi(\mathbf{r}_i, \mathbf{r}_I, t) = E\Psi(\mathbf{r}_i, \mathbf{r}_I, t) \quad (2.5)$$

Here, H , Ψ , and E are the Hamiltonian operator, wave function, and system energy, respectively. The variables \mathbf{r}_i and \mathbf{r}_I are coordinates of the electron and nucleus respectively. t represents time.

Attention had been focused on solving the Schrödinger equation for decades but the complexity of the system made this difficult. However, with the following approximations [26, 30, 31], the Schrödinger equation can be simplified and solved.

1. Only deal with the ground states of electrons at 0K, thus we do not need to consider time, since the ground state is time-independent.

2. Since the electron's mass is extremely small and its speed is much slower than light, the gravity and relativity can be ignored.

3. Nuclei are far more massive than electrons. Thus, electrons will respond to nucleus' motion instantaneously while the nucleus is not much altered by electron motion. It is thus possible to fix the positions of lattice nuclei approximately with respect to the motion of electrons. Born-Oppenheimer approximation decouples the Schrödinger equation into the electronic and nuclear components: $E_{\text{atom}} = E_{\text{nucleus}} + E_{\text{electron}}$.

Based on the above approximations, one can simplify the Schrödinger equation to

$$H\Psi(\mathbf{r}) = E\Psi(\mathbf{r}) \quad (2.6)$$

Here \mathbf{r} is the electronic coordinate.

2.2.1.2 Energy Operator: Hamiltonian

The Hamiltonian operator in Eq. (2.6) includes kinetic energies of nuclei (E_I^{kin}) and electrons (E_i^{kin}), and potential energies from nucleus-electron (U_{Ii}), electron-electron (U_{ij}) and nucleus-nucleus (U_{IJ}) interactions. It can be written as:

$$H = E_I^{\text{kin}} + E_i^{\text{kin}} + U_{Ii} + U_{ij} + U_{IJ} \quad (2.7)$$

According to assumptions in 2.2.1.1 section, terms correlated with nuclei can be skipped and therefore, we only need to focus on electrons:

$$H = E_i^{\text{kin}} + U_{Ii} + U_{ij} \quad (2.8)$$

2.2.1.3 Many electron problem

With the above approximations, Schrödinger equation can be solved for simple systems such as an electron in a well and hydrogen system. However, for materials containing $10^2 \sim 10^3$ atoms or electrons, the computer has difficulty to handle. It is too complicated to deal with so many electrons at the same time. Thus, several simplified models are proposed to address this issue.

Hartree [32] assumes that each electron is independent and interacts with each other in an average way. The total energy is the sum of each single electron energy, and total wave function is a product of single electron work functions. Schrödinger equation for a single electron is expressed as

$$\left(-\frac{1}{2} \nabla^2 + U_{\text{ext}}(\mathbf{r}) + U_{\text{H}}(\mathbf{r})\right) \Psi(\mathbf{r}) = E \Psi(\mathbf{r}) \quad (2.9)$$

The first term is the kinetic energy, U_{ext} is the interaction between nuclei and electrons, and U_{H} is the Hartree potential coming from classical Coulomb repulsive interaction between each electron and the mean field and can be obtained via Poisson equation: $\nabla^2 U_{\text{H}}(\mathbf{r}) = -4\pi\rho(\mathbf{r})$.

Based on Hartree method, Hartree-Fork method [33] approximates the wave function as a linear combination of non-interacting one-electron wave functions in the form of a Slater determinant to make it more perfect. In this method, we have $\Psi(\mathbf{r}_1, \mathbf{r}_2) = -\Psi(\mathbf{r}_2, \mathbf{r}_1)$ and $\int \Psi^* \Psi d\mathbf{r} = 1$ after normality. Wave function is written as

$$\left(-\frac{1}{2} \nabla^2 + U_{\text{ext}}(\mathbf{r}) + U_{ij}(\mathbf{r})\right) \Psi(\mathbf{r}) = E \Psi(\mathbf{r}) \quad (2.10)$$

The expression for energy equation after integration is

$$E = \frac{\int \Psi^* H \Psi d\mathbf{r}}{\int \Psi^* \Psi d\mathbf{r}} = \int \Psi^* H \Psi d\mathbf{r} = \sum_{i,j} \int \Psi_i^*(\mathbf{r}) \left(-\frac{1}{2} \nabla_i^2 + U_{\text{ext}}(\mathbf{r}) + U_{ij}(\mathbf{r}) \right) \Psi_j(\mathbf{r}) d\mathbf{r} \quad (2.11)$$

The first two terms are only related to one electron coordinate while the third term, $U_{ij}(\mathbf{r})$, depends on two electronic coordinates. After integration, it will result in two energy terms. The energy could be expressed as:

$$E = E_{\text{kin}} + E_{\text{ext}} + E_{\text{H}} + E_{\text{x}} \quad (2.12)$$

Where E_{x} is a new term compared with Hartree's method and it has negative energy, implying that like-spin electrons avoid each other and keep some distance.

2.2.1.4 Variational principle to search for ground state

Ground state is unique for a given system and given conditions. It has the lowest energy, so by minimizing the system energy, the energy at the end will be the ground-state energy. At ground state, we have

$$\delta \left(\int \Psi^* H \Psi d\mathbf{r} \right) = 0 \quad (2.13)$$

2.2.2. Density Functional Theory

Although several approximations are listed in Section 2.1, first-principles calculation is still limited in practical application. However, the density functional theory (DFT) based on a fictitious system eventually has made it possible to solve many electron problem for complex systems.

2.2.2.1 Hohenberg-Kohn Theorem

Hohenberg and Kohn [34] developed two theorems to designate the electron density

as the key in DFT, which builds bridges between electron density, external energy, Hamiltonian, and wave function.

The first theorem states that external potential, U_{ext} , refers to the interaction between nuclei and electrons, which is system-dependent. This interaction is only determined by the ground-state electron density, which could be expressed as $E_{\text{ext}}[\rho(\mathbf{r})]$. Other terms in Eq. (2.12) are related to system-independent internal potential (electron kinetic energy and electron-electron potential) and can be expressed by a universal functional $F[\rho(\mathbf{r})]$. For a system with a given external potential at ground state, the electron density is sufficient for solving the total energy by: $E[\rho(\mathbf{r})] = F[\rho(\mathbf{r})] + E_{\text{ext}}[\rho(\mathbf{r})]$.

The second theorem proves the variational principle in the framework of DFT. By minimizing the system energy, one can find the ground state.

$$E[\rho(\mathbf{r})] = F[\rho(\mathbf{r})] + E_{\text{ext}}[\rho(\mathbf{r})] \geq E_{\text{gs}} \quad (2.14)$$

The electron density, $\rho(\mathbf{r})$, is a 3-dimensional density of electrons, $\rho(x, y, z)$. Thus, for a n-electron problem, 3n-dimensional equations are simplified to n separate 3-dimensional ones, which makes the calculation much easier.

2.2.2.2 Kohn-Sham Equation

The electronic kinetic energy in terms of electron density is poorly represented in early years, which limited the application of first-principles calculations. Kohn and Sham [35] constructed a fictitious system of non-interacting electrons which generate the same density as any given system of interacting particles, in DFT, and thus solved this problem.

Since each electron was assumed to be noninteracting, energies are decomposed into:

$$E_{\text{kin}} = E_{\text{kin}}^{\text{non}} + E_{\text{kin}}^{\text{int}} \quad (2.15)$$

$$E_{\text{H}}+E_{\text{x}} \rightarrow E_{\text{H}}+E_{\text{x}}+ E_{\text{c}}^{\text{int}} \quad (2.16)$$

Use E_{xc} to represent the exchange-correlation energy, $E_{\text{x}}+ E_{\text{c}}^{\text{int}} + E_{\text{kin}}^{\text{int}}$, the final expression for the total energy in Eq. (2.12) becomes:

$$E = E_{\text{kin}}^{\text{non}} + E_{\text{kin}}^{\text{int}} + E_{\text{ext}} + E_{\text{H}} + E_{\text{x}} + E_{\text{c}}^{\text{int}} = E_{\text{kin}}^{\text{non}} + E_{\text{ext}} + E_{\text{H}} + E_{\text{xc}} \quad (2.17)$$

In this way, the first three items are easy to be calculated. The last item is unknown and needs approximation. In the Kohn-Sham system, the Hamiltonian is expressed as:

$$H_{\text{KS}} = E_{\text{kin}}^{\text{non}} + U_{\text{ext}} + U_{\text{H}} + U_{\text{xc}} = -\frac{1}{2} \nabla^2 + U_{\text{eff}} \quad (2.18)$$

Where U_{eff} is the effective potential, which gives the same energy and electron density of the non-interacting electronic system as those of a true interacting system.

2.2.2.3 Exchange-Correlation (XC) functionals

In DFT, how to construct or choose the XC functional will affect the accuracy of calculation. If the XC functional is improperly chosen, the connection between true n-electron and fictitious one-electron systems will be lost and the results will be unreliable.

Most used XC functionals include local density approximation (LDA) and generalized gradient approximation (GGA). LDA works well in covalent systems

and simple metals, where the variation in charge density is relatively slow but not reliable to adsorption energies or energy barriers. GGA was developed to generate more accurate XC functionals. It overcome the deficiency of LDA and was more widely applied.

2.2.2.4 Iterative variational approach

The variational principle is conducted in the following scheme:

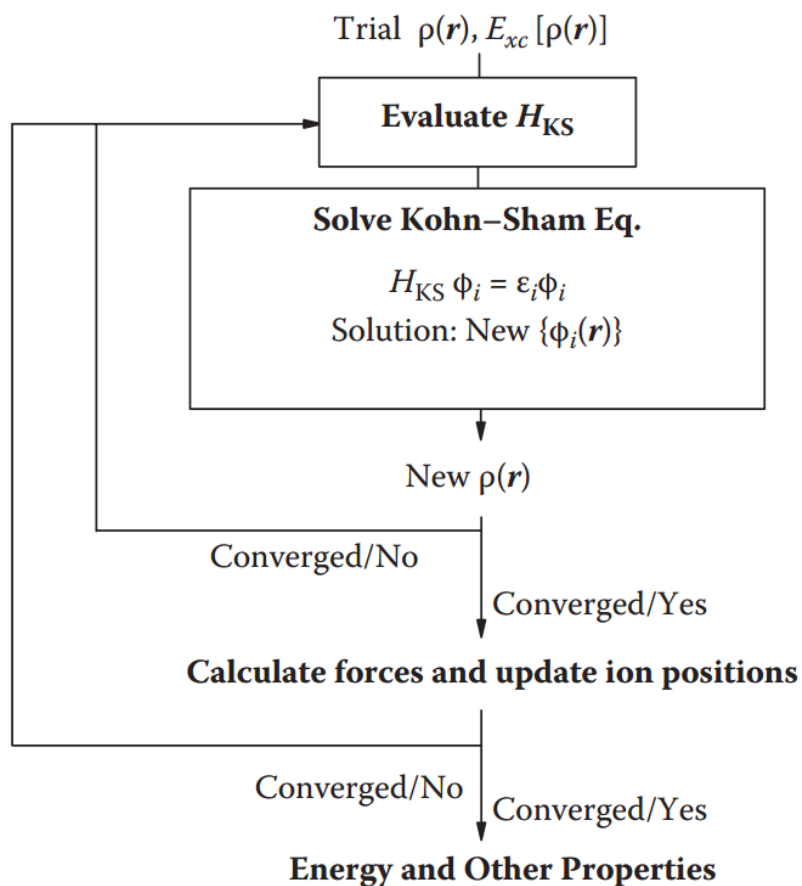


Figure 2.2 Schematic of a typical DFT procedure by iterative self-consistent loop [27].

2.2.3 Pseudopotentials (PPs)

Frozen-core approximation divides electrons surrounding a nucleus into core electrons and valence electrons. Core electrons are stable and valence electrons are active. Thus, simplified pseudopotentials can be used to replace all-electrons potentials to reduce the number of plane waves needed for the expansion of a pseudo wave function. Most DFT codes provide PPs for all isolated atoms. They can be used as simple as just adding them up, regardless of whether it is used for single atom, molecule, or bulk solid.

Three common types of PPs are normal conserving PPs, ultrasoft PPs (USPPs), and projector-augmented wave (PAW) PPs. The one used in this research is PAW. It is proposed by Blochl in 1994 [36] and adopted by Kresse and Joubert [37] in 1999. These PPs possess both efficiency of the PP and the accuracy of all-electron potentials.

3 A Microscale Dynamic Model for Wear Simulation of Core-shell Structured High Cr Cast Irons

This chapter reports a computational study on effect of core-shell structured carbides on wear of high-Cr cast irons, using the MSDM.

3.1 The modeling procedure

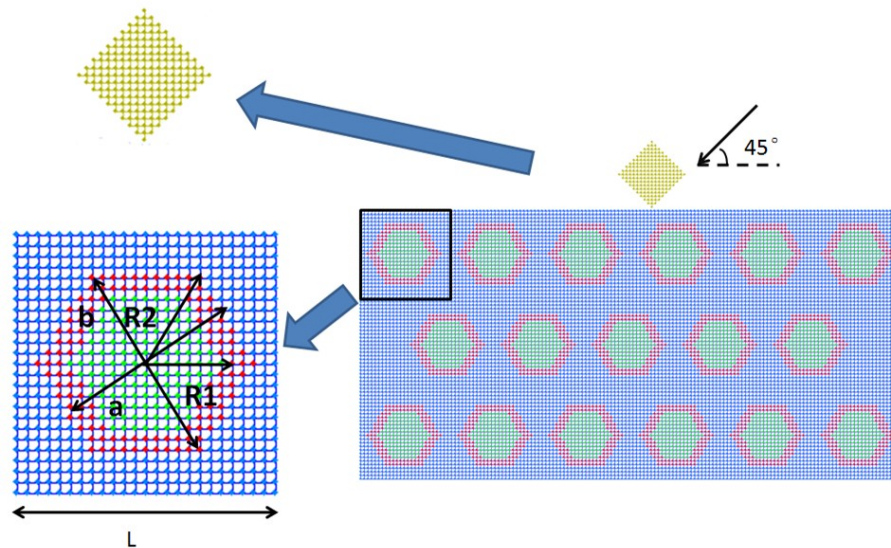


Figure 3.1 A model system used for simulation. The core-shell hexagon represents the M_7C_3 core (green) surrounded by $M_{23}C_6$ shell (red). $R_1=14\mu m$, $R_2=20\mu m$; The thickness ratio of core to shell is about 2.3:1. The yellow square represents an ejected erodent particle. The shape of the carbide can be modified for more general situations.

For the MSDM modeling, Visual Studio 2010 professional (Microsoft) was used, and all components were written in C++. The microstructure of 45-4 HCCI (Fe-45%Cr-4%C) consists of ferrite and carbides (single-phase carbide: M_7C_3 ; or core-shell structured carbide: $M_7C_3(\text{core})-M_{23}C_6(\text{shell})$). Fig. 3.1 illustrates a model system. Mechanical properties of various phases in the microstructure are given in Table 3.1 [11]. The target material is discretized and mapped on a lattice consisting of 6×3 units. Every unit contains 25×25 sites, as shown in Fig. 3.1. The carbide is designed as a hexagon according to SEM images reported [3, 4, 7]. The length of each bond (l_0) between a pair of adjacent site is 2×10^{-6} m, and time interval (Δt) is set as 8×10^{-11} s based on theoretical consideration for MSDM modeling [20]. For the carbide/matrix interfaces, both M_7C_3 and $M_{23}C_6$ are assumed to have similar chemical bonds or chemical interactions with the ferrous matrix. Thus, the difference in the overall carbide/matrix interfacial bond strength between M_7C_3 and $M_{23}C_6$ is mainly determined by the mechanical mismatch or the difference in mechanical properties between the carbide and the matrix. When an erodent particle is approaching the target surface and the distance between a site on the target surface and that of the particle is smaller than l_0 , an interaction force is generated as $\vec{J} = \kappa \cdot \Delta \vec{v} = E_m \cdot \nu_0 \cdot \Delta \vec{v}$ between this pair of sites. E_m in this equation is the Young's modulus of target material on surface. In order to compare the performance of core-shell carbide with that of single-phase carbide, carbides are uniformly distributed in the matrix in the same way as Fig. 3.1 illustrates. The same spatial arrangement of two types of carbides in the model systems allows comparing their performances during erosion under the same condition. If we randomly distribute

carbides with different sizes, similar to realistic situation, the simulated wear condition will not be the same and the presented comparison would lead to misleading information unless the system is sufficiently large for satisfactory statistical analysis.

Table 3.1 Mechanical properties of the modeled materials [11].

Material	E(Gpa)	Yield stress(MPa)	Tensile strength(MPa)	Fracture strain(%)
SiC	430	860	860	0.2
Ferrous matrix	200	400	640	30
Shell($M_{23}C_6$)	500	1000	1080	0.36
Core(M_7C_3)	700	1400	1400	0.2

In order to save computing time, square particle with a certain angularity is used as the erodent, which generates a larger impact force and is easy to simulate. The orientation of particle relative to the surface is kept constant for all situations. A sand particle has 181 sites with the square length of approximately 2.5×10^{-5} m. For two-dimensional modeling, a square particle is more erosive than a circular spherical. Although in experiments, slurry, a mixture of water and sand was used, the model in this study does not consider the effect of water which influences the erosive force, since the main objective of the modeling is to investigate how the core-shell structure generally helps resist carbide/matrix interfacial failure under impact force.

The velocity of the erodent particle was set as 8m/s, and the impingement angle was

set as 45° relative to the sample surface. The modeling condition was set based on reported experimental testing [7], in which the experiments were performed using a slurry pot erosion tester and the slurry was tap water mixed with silica sand (12–50 mesh, Manus Abrasive Systems Inc., Edmonton, Canada). The experiments show that Fe-45Cr-4C alloy with core-shell structured carbides exhibits the highest erosion-corrosion resistance. We cite the reported experiments to show the consistence between the modeling work and the experimental observation rather than to make quantitative comparison, since the condition for the simulated erosion tests cannot be the same as that for the experiments. For each computational erosion test, 8 particles were used to strike the target surface at random locations in a certain central area. The particles were ejected one by one, so that there was no interaction between ejected particles. Each set of simulations was repeated for five times, from which an average value was calculated and reported in this article.

It should be mentioned that the reported is a 2D modeling study, which may be regarded as a study for the plain strain situation. 2D micro-scale dynamic modeling has been applied to investigate abrasive wear[22] and solid-particle erosion of composite materials[20]. Results of the modeling studies and experiments are consistent, indicating that the 2D modeling can reflect the trend of 3D situations. In this study, we conducted 2D modeling with the intent to demonstrate the benefits of core-shell structured carbides to the erosion resistance rather than providing accurate quantitative information, since the geometry of realistic 3D carbide varies with individual carbides and it is difficult to simulate and cover all different cases.

3.2 Stress/strain analysis using FEM

Stress/strain distributions around the core-shell carbide and single-phase carbide under the external force were analyzed using the finite element method. This part of work was carried out in collaboration with Dr. H. Guo, a visiting scholar from Taiyuan University of Science and Technology. Fig. 3.2 illustrates a core-shell carbide embedded in a ferrous matrix. The dimensions of the model system were $0.2 \times 0.2 \times 0.2 \text{mm}^2$. Different thickness values of the shell were analyzed through the static structural analysis using Mechanical APDL Solver in ANSYS Workbench 15.0. The thickness of shell was changed in order to see how the ratio of the shell thickness to the core dimensions influenced the stress and strain states.

Mechanical properties of the materials used for the stress/strain analysis are presented in Table 3.1. The element dimensions are $0.2 \times 0.2 \times 0.2 \text{mm}^3$. This size is chosen to have the FEM element the same as that of the MSDM model, which has its square element's dimensions equal to 0.2×0.2 (Fig. 3.1). A vertical force was applied to the target surface by pressing a rigid hemispherical indenter onto the surface. The material of indenter is WC and the boundary conditions for the FEM analysis are the same as those for the MSDM modeling with a fixed bottom of the model system. The target materials involved the FEM analysis are the same as those for the MSDM modeling, namely, the matrix is ferrous and the shell and core of carbide are M_{23}C_6 and M_7C_3 , respectively. Properties of the materials are given in Table 1.1.

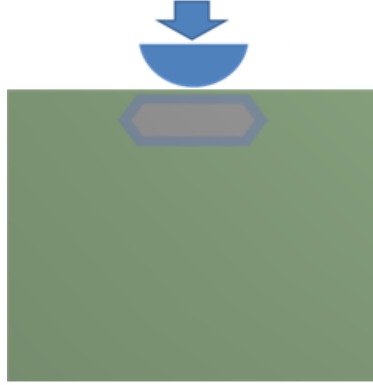


Figure 3.2 A cross-sectional view of a FEM model for analyzing stress/strain distribution around a core-shell carbide in comparison with a single-phase carbide (i.e. shell thickness = zero).

3.3. Results and discussion

3.3.1 Effects of the core-shell structured carbides on erosion of HCCIs

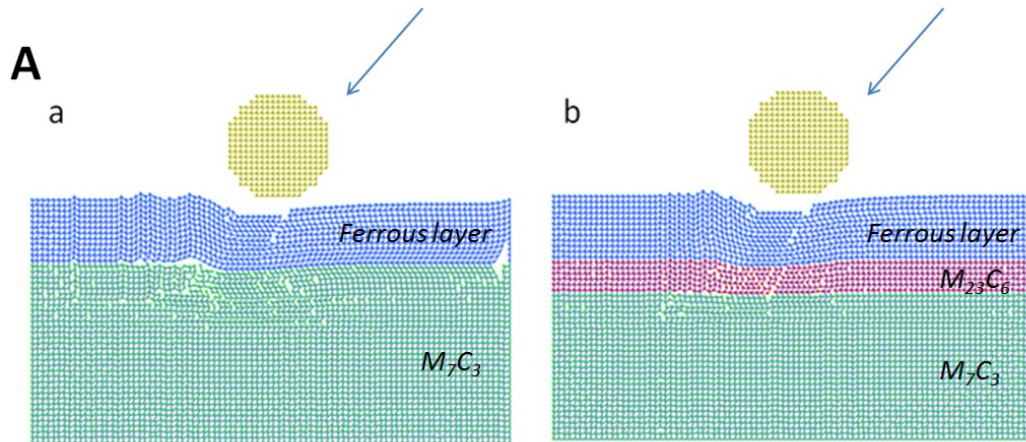
3.3.1.1 Solid particle erosion and the performance of the core-shell carbide

Computational solid-particle erosion tests for HCCI systems with core-shell structured carbides and single-phase carbides, respectively, were performed. In order to view the local damage caused by erodent striking, M_7C_3 -ferrous matrix and M_7C_3 - $M_{23}C_6$ -ferrous matrix layered systems, which simulate the local core-shell structure, were first analyzed.

As shown in Fig. 3.3A, the core-shell carbide leads to reduced local interfacial

cracking, compared to the one without the intermediate layer of $M_{23}C_6$. Corresponding material losses were also counted. Fig. 3.3B presents the results obtained from the simulation and previous experimental data for comparison. As shown, the core-shell structured carbides decrease the volume loss, which is consistent with the experimental observation [7]. Such a decrease is ascribed to lowered probability of interfacial cracking due to reduced mechanical mismatch when a medium hard carbide shell existed between the hard core carbide and the ferrous matrix. As demonstrated by FEM analysis shown in section 3.3.2, the core-shell structure helps minimize the interfacial stress and thus lowers interfacial fracture.

It may need to mention that for modeling the systems shown in Fig. 3.3, spherical particles were used to impinge the surface. Using the spherical particle was to avoid local stress concentration, which could cause more top surface damage without affecting much the interface between the metallic layer and the carbide.



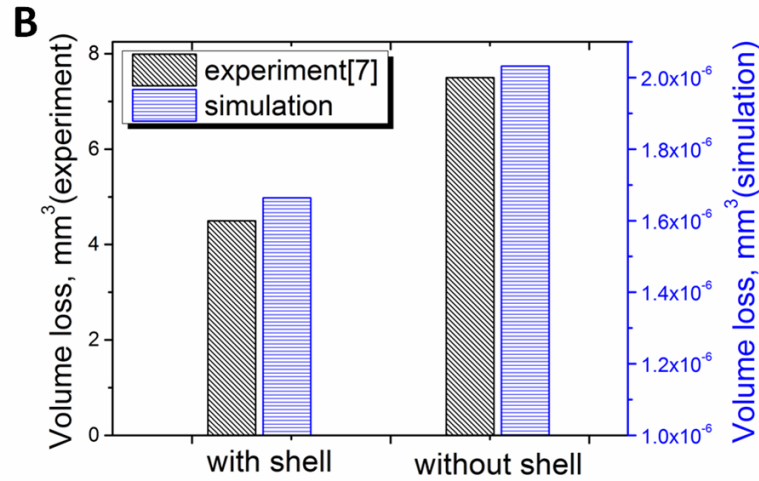


Figure 3.3 A. (a) A system consisting of iron and M_7C_3 layers struck by a spherical solid particle at an angle of 45° with a velocity of 4.0m/s, and (b) a system consisting of iron, $M_{23}C_6$ and M_7C_3 layers under the same striking condition. **B.** Material losses caused by erosion (modeling and experimental).

3.3.1.2 Influence of the shell thickness on erosion

The beneficial effect of the core-shell structured carbides should be influenced by the shell thickness, which can be controlled through destabilization heat treatment[9, 38]. It is believed that $M_{23}C_6$ is transformed from M_7C_3 through nucleation and growth on the original M_7C_3 in the ferrous matrix [3]. Thus, with the possibility of modifying the shell thickness, it is of importance to investigate how the shell thickness influences erosion in order to optimize the core-shell configuration. In this study, effects of several thickness values of $M_{23}C_6$ shell, including 6um, 8um, and 10um, on erosion were modeled with the size of entire carbide kept the same.

Results of the modeling are shown in Fig. 3.4A. As illustrated, as the shell becomes thicker, the erosion loss decreases initially but later increases after reaching a minimum. The minimum point occurred at the thickness of 8 μ m. Such a trend is understandable since although shell can reduce interfacial fracture, too much $M_{23}C_6$ sacrifices the hardness of carbide. Corresponding changes in system's configuration caused by erosion are illustrated in Fig. 3.4B.

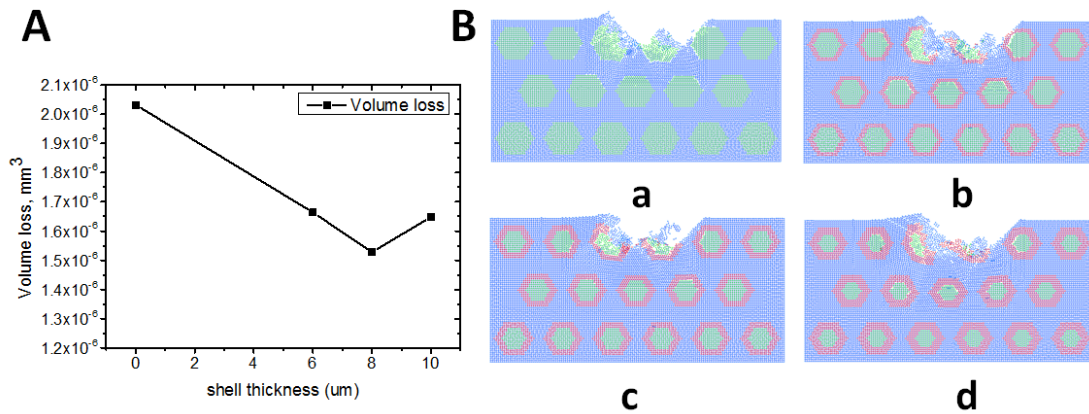


Figure 3.4 A - Influence of the shell thickness on erosion; B - Corresponding configurational changes caused by erosion of HCCI samples containing core-shell carbides with different shell thickness values: (a) 0 μ m, (b) 6 μ m, (c) 8 μ m, and (d) 10 μ m. The impingement angle is 45°.

3.3.1.3 Influences of carbide shape and orientation on erosion

Gao, et al. [39] applied thermo-mechanical treatments to high-Cr cast irons and showed that carbide's shape and orientation can be controlled through the treatments. In this computational study, further simulation was conducted to see how the

carbide shape and orientation affect erosion. Fig. 3.5B illustrates erosion of several systems with their core-shell carbides having different ratios of the length to width of the carbide i.e. a/b ratio, which are equal to 3, 2, 1, $1/2$ and $1/3$, respectively. Five particles were used to strike the central area randomly. Corresponding material losses or volume loss of the five systems are illustrated in Fig. 3.5A.

As shown, the erosion loss increases as the a/b ratio decreases. Or alternatively, when the elongated carbides are aligned in parallel to the impingement direction, the erosion loss is the minimum. Uniaxial carbide does not necessarily perform better than elongated ones, depending on the carbide orientation. Such a trend could be explained as follows. The carbide parallel to the sand impingement direction performs better, since its dimension along the impingement direction is large, which helps withstand the load. Besides, the surrounding matrix provides more effective confinement to the carbide, helping suppress cracking in the carbide. In contrast, when the carbide is perpendicular to the impingement direction, the brittle carbide close to surface may experience more direct impact and thus has a higher probability of fracture. Similar trend was demonstrated in previous studies on carbon steel [25].

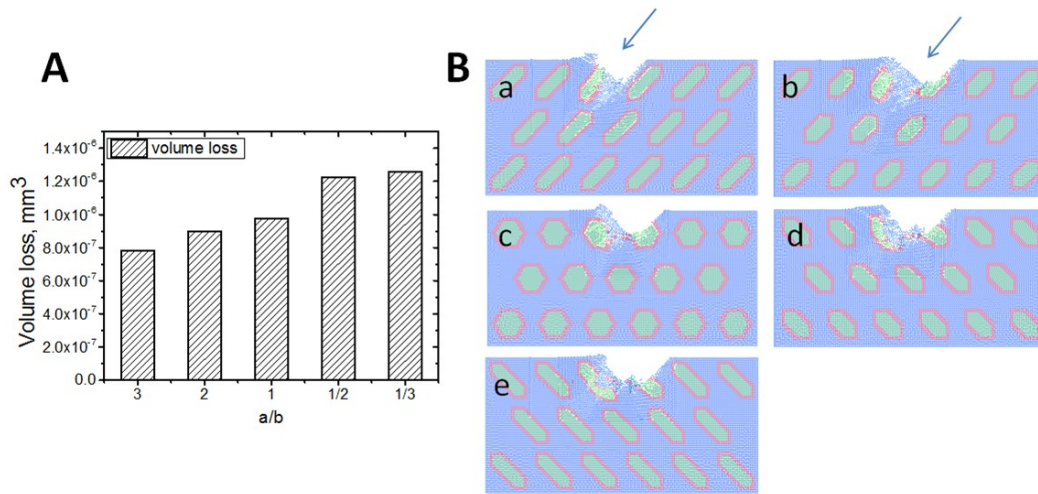


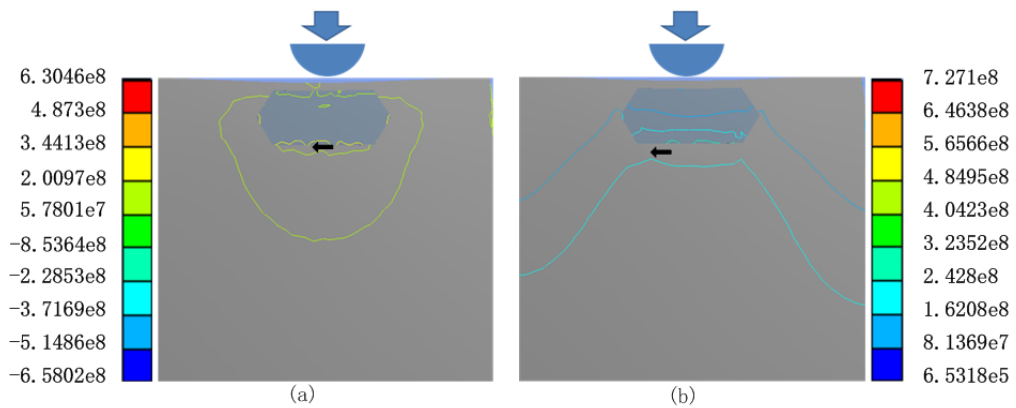
Figure 3.5 A - Five carbide configurations were used to investigate influences of carbide shape and orientation on wear loss; Impingement angle = 45° and the ratio of length to width of carbide, i.e. a/b ratio, are (a) 3, (b) 2, (c) 1, (d) 1/2 and (e) 1/3. **B** - Site losses of the five model systems under the same erosion condition.

3.3.2 Effects of the core-shell structure and carbide orientation on stress and strain distributions

3.3.2.1 Influence of the core-shell structure on stress distribution

Stress/strain analysis was conducted in collaboration with Dr. Guo using the finite element method for more information on the benefits of core-shell structured carbide on the resistance to erosion. For comparison, both core-shell structured ($M_7C_3 - M_{23}C_6$) and single-phase (M_7C_3) carbides were analyzed. The size of the carbides was kept constant, so that the thicker the shell, the smaller the core. For present analysis, an elongated carbide was lied horizontally as illustrated in Fig. 3.2,

which was pressed under a pressure of $6.5 \times 10^8 \text{ Pa}$. Figs. 3.6(a) and 3.6(b) illustrate isolines of principle stress and shear stress around a carbide without the M_{23}C_6 shell, while Figs. 3.6 (c) and 3.6(d) show isolines around a core-shell structured carbide with its shell thickness equal to 4 microns. It was observed that the maximum principal stress was located in the central area of the bottom carbide/matrix interface as indicated by the arrow. The core-shell structured carbide reduced the maximum principal stress from $6.3 \times 10^8 \text{ Pa}$ to $2.4 \times 10^8 \text{ Pa}$, and the maximum shear stress from $7.3 \times 10^8 \text{ Pa}$ to $5.0 \times 10^8 \text{ Pa}$. Such decreases in stress indicate that the core-shell helps increase the stress-bearing capability of the carbide.



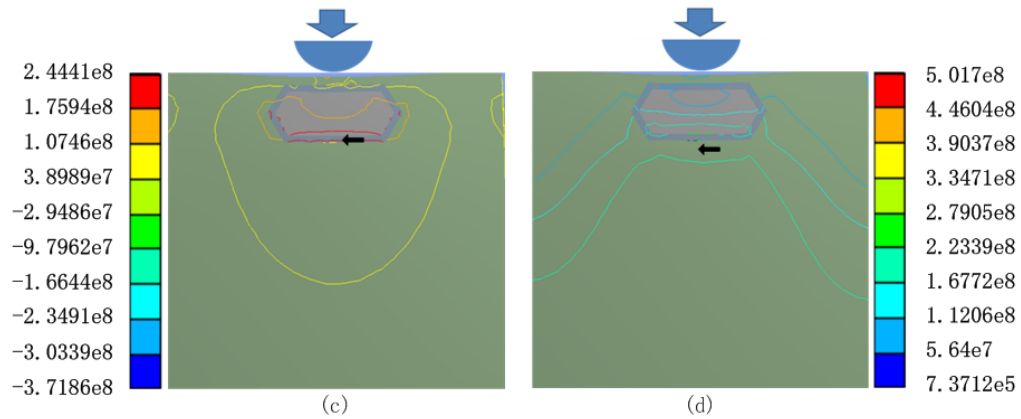


Figure 3.6 (a) Isolines of principal stress around a M_7C_3 carbide, (b) isolines of shear stress around the M_7C_3 carbide; (c) isolines of principal stress around a core-shell carbide, and (d) isolines of shear stress around the core-shell carbide.

3.3.2.2 Influence of the carbide orientation on stress distribution

Stress distributions around vertically and horizontally lied carbides were analyzed. Since it is clear that the core-shell structured carbide can reduce stress, only the core-shell structured carbide was analyzed here. Figs. 3.7(a) and 3.7(b) illustrate isolines of the principal stress around the carbide with its shell thickness equal to 4 microns. Results of the analysis show that the maximum principle stress of the vertically lied carbide is $3.2 \times 10^8 Pa$, which is larger than that of the horizontally lied one ($2.4 \times 10^8 Pa$). The max stress at the vertically lied carbide is concentrated in a small region while that at the horizontally lied one spreads in a wider range. According to the FEM analysis, the horizontally lied carbide with smaller maximum principal stress could result in a higher erosion resistance, which is contradictory to the result shown in Fig. 3.5. However, because of the lying direction and matrix

confinement, the horizontally lied carbide could suffer from bending and interfacial debonding, thus likely triggering global failure; while the vertically lied one may suffer more from local damage but has a lower probability for crack spreading. Fig. 3.8 schematically illustrates such possible situations. The conclusion of higher erosion resistance with vertically lied carbides shown by the modeling study is consistent with the phenomenon previously reported by Coronado [40], who observed that a sample with its rod-like carbides vertical to surface showed its wear resistance 10% higher than that with its carbides parallel to the surface.

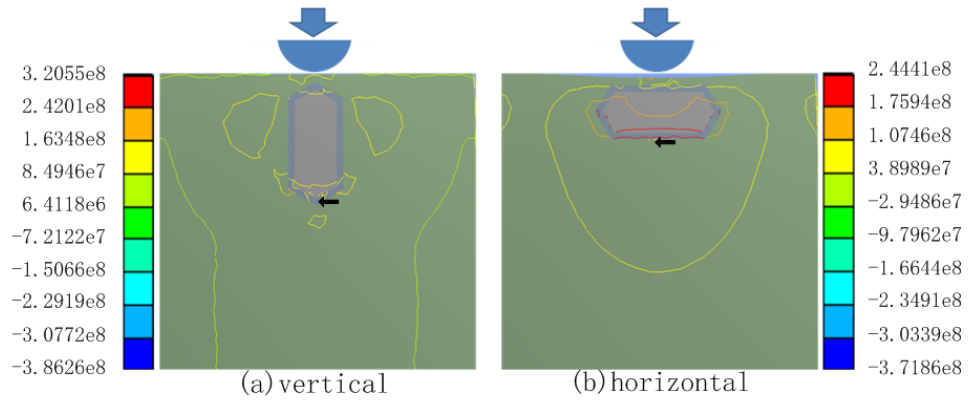


Figure 3.7 Isolines of principal stress for vertically and horizontally aligned carbides.

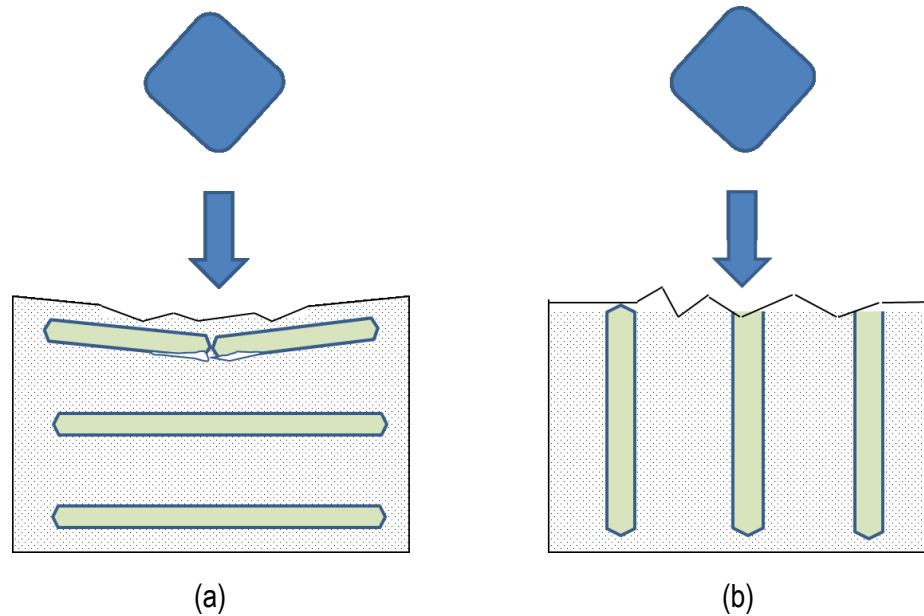


Figure 3.8 Schematic illustration of two possible situations: (a) the horizontally lied carbide could suffer from bending and interfacial debonding, thus likely triggering global failure; (b) the vertically lied one may suffer more from local damage but has a lower probability for cracking spreading.

3.3.2.3 Influence of the shell thickness

The thickness of $M_{23}C_6$ shell certainly influences the stress distribution. The stress distributions around core-shell carbides with different shell thickness values ranged from 0 to 12 microns were analyzed. The values of zero and 12 microns correspond to M_7C_3 and $M_{23}C_6$ carbides, respectively. Fig. 3.9(a) and (b) illustrate variations in maximum principal stresses and shear stresses with respect to the shell thickness. For vertically aligned carbide, both the maximum principal stress and shear stress descend as the shell thickness increases as Fig. 3.9(a) illustrates. They became approximately saturated when the shell thickness reaches a certain level. However,

the situation changes for the horizontally aligned carbide. As observed (Fig. 3.9 (b)), both the maximum principal and shear stresses decrease first, then increase and finally saturated as the shell thickness increases. In this case, the saturated principal and shear stresses are still lower than those of the carbide without the $M_{23}C_6$ shell. The obtained information would help maximize the benefit of the core-shell structured carbide by controlling the shell thickness. The results indicate that the softer shell helps minimize the stress at the carbide/matrix interface and thus lowers the probability of interfacial failure. However, if the shell is too thick, such benefit may diminish and the carbide would not be strong enough to play the role as an effective reinforcing phase.

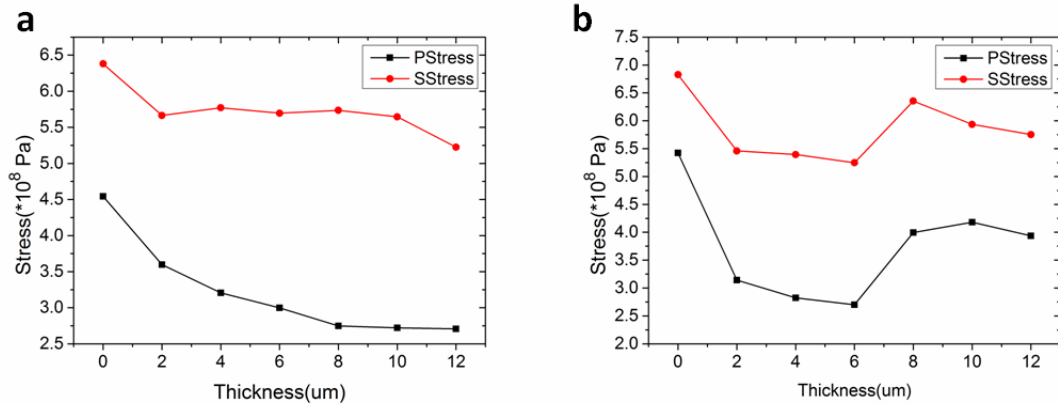


Figure 3.9 Variations in maximum principal and shear stresses with respect to the shell thickness. (a) Vertically aligned carbide; (b) Horizontally aligned carbide.

3.4 Summary

Recent studies show that core-shell structured carbides in high-Cr cast irons (HCCIs)

are beneficial to the resistance of materials to wear. In order to maximize such benefit, a computational study was conducted to determine how the erosion resistance of HCCIs was influenced by the core-shell structure, shell thickness, carbide shape and orientation geometry using a micro-scale dynamic model. FEM method was also employed for analyzing stress and strain distributions near carbide/matrix interfaces. The FEM study provides supplementary information for better understanding of underlying mechanisms. Results of the study demonstrate that

- 1) The softer shell helps minimize the stress at the carbide/matrix interface and thus lowers the probability of interfacial failure.
- 2) Elongated carbides aligned in the particle impingement direction perform better than those which are perpendicular to the impingement direction.
- 3) For vertically aligned carbide, both the maximum principal and shear stresses decrease as the shell thickness increases and become approximately saturated when the shell thickness reaches a certain level.
- 4) For horizontally aligned carbides, both the maximum principal and shear stresses decrease first, then increase and finally saturated as the shell thickness increases.
- 5) If the shell is too thick, such benefit may diminish and the carbide would not be strong enough to play the role as an effective reinforcing phase.

4 Understanding Effects of Cr content on the Slurry Erosion behavior of High-Cr cast irons through Local property mapping and Computational analysis

Besides changing morphology of carbides, HCCIS can be optimized by adjusting chemical compositions. Information on microstructure from previous SEM characterization obtained by Dr. X. H. Tang does not provide sufficient clues for understanding the slurry erosion behavior of HCCIs evaluated by Dr. Reinaldo [41]. Thus, local properties including Young's modulus and electron work functions are measured for individual phases in this study to understand the mechanism. Besides, first-principles calculation for carbides and matrix are conducted to understand the effect of Cr.

It appears that adding chromium can endow cast iron with higher resistance to erosion-corrosion since it helps form carbides and enhance corrosion resistance of matrix. However, whether this trend is applicable to all HCCIs needs to be investigated, since the Cr content may affect compositions of carbides and matrix, leading to variations in their properties.

Regarding properties of M_7C_3 carbide, it is noticed that the Cr/Fe ratio affects the hardness of $(Fe, Cr)_7C_3$ carbide. The calculation by Zhang et al. [1] shows that $Fe_4Cr_3C_3$ has the largest elastic modulus and hardness among all $(Fe, Cr)_7C_3$ carbides with different Cr/Fe ratios. Xiao et al. [42] also computationally

demonstrate that the elastic modulus of $Fe_{16}Cr_{12}C_6$ is larger than that of Cr_7C_3 . Thus, it is worth investigating and determining the optimal Cr content for maximized benefits from the high-Cr cast irons through adjusting the Cr/Fe ratio.

The alloyed chromium should also affect the mechanical properties of the matrix through solid-solution strengthening mechanism. Furthermore, Cr renders the ferrous alloy resistant to corrosion, leading to elevated resistance to erosion-corrosion. Thus, it is of importance to understand such effects in order to maximize the benefits from alloyed chromium.

In this study, effects of chromium content, in the range of 5~35%Cr, on the performance of HCCIs containing 5%C during erosion tests in slurries with two pH values and four velocities were investigated. Local mechanical properties and electron work function which is related to the surface energy and reflects the stability of a surface and its anti-corrosion capability, were analyzed for both the ferrous matrix and $(Fe,Cr)_7C_3$ carbides using a micro-indenter and a multi-mode atomic force microscope. First-principles calculation was conducted to analyze $(Fe,Cr)_7C_3$ carbides and the matrix to understand mechanisms responsible for observed phenomena.

4.1 Experiment Details

4.1.1 Sample Preparation

Materials under study are cast irons containing 5%C and Cr with its concentration from 5% to 35%, balanced by Fe and minor elements (Mn: 2.2~2.8 wt% and Si: 0.8~1.4 wt%). Ingots of the alloys were made using an induction furnace, from which specimens (10mm×10mm×1mm) were cut for microstructure characterization. The surface of specimen was wet ground with SiC papers (up to 2000 grit), and then polished using diamond paste (~ 0.5 μm). After the mechanical polishing, the specimens were etched using a solution of picral solution for 2 seconds in order to remove residual deformation or stress in the surface layer introduced by the mechanical polishing as well as for revealing microstructure features. The specimens were ultrasonically cleaned in ethanol and dried in a N₂ gas flow. In order to understand the role that Cr plays in affecting properties of the alloys, samples containing 5%Cr, 10%Cr, 20%Cr and 35%Cr, respectively denoted as #5-5, #10-5, #20-5 and #35-5 were selected for analyzing their local electron work function and Young's modulus. The work function is the minimum energy required to extract electrons from the interior of a solid to its surface without kinetic energy. It is a fundamental measure of electrochemical stability and has been related with alloy's mechanical properties and anti-corrosion properties [43, 44]. For slurry erosion tests, samples with dimensions of 9mm×5mm×50 mm were used.

4.1.2 Slurry erosion testing

For applications of HCCIs in slurry transport for the oil sand operation, slurry erosion tests were carried out using a home-made slurry-pot tester. The tester had a cylindrical tank of 29 cm in diameter and 22 cm in height. In the tank, four baffles were mounted on the internal wall to block the slurry flow so that the samples

would travel in the slurry at a velocity that was equal or close to the nominal velocity. A slurry solution consisting of 20 Vol.% silica sand (sand particle size: 500 μm in diameter) and 80 Vol.% water was placed in the slurry container. pH value of the solution was adjusted by adding HCl. Samples (9mm \times 5mm \times 50 mm) were held by a holder, which was connected to a motor that rotated during erosion test and thus drove the samples to move in the slurry. The sand impingement angle was set to be 45° and the moving velocity was 2.5, 5.0, 6.5 and 8.0m/s respectively. For each slurry-erosion test, the total distance that samples travelled in the slurry was 15km. With initial deviation assessment, it was turned out that the distance of 15 Km was sufficient for obtained repeatable results. Standard deviations were generally in the range of $\pm 10\%$ for our slurry-pot erosion testing arrangement for HCCIs. After the test, the samples were rinsed and lightly brushed to remove corrosion products and then further cleaned by rinsing with distilled water. The weight loss of each sample was measured using a balance with a precision of 0.1 mg. More details about the home-made slurry pot erosion tester and the experimental set-up can be found in previous publication [45].

Electron work function and reduced Young's moduli of carbide and matrix were mapped using a Bruker MultiMode atomic force microscope (AFM)8 with PeakForce KPFM capability. The modulus given by AFM is a reduced Young's Modulus by fitting the retract curve using the Derjaguin, Muller, Toropov (DMT) model [46]. Bruker magnetic probes (MESP) with its force constant of 2.8 N/m were used for measuring the modulus and work function. The purpose of *in situ* mapping both work function and the reduced modulus is to view the relation

between the modulus and work function.

For more precise information, a micro-indenter (Fischer Technology, Inc., Windsor, CT, USA) was employed to measure micro-hardness and Young's modulus for carbides and matrix in the HCCIs under a load of 1N. The overall hardness or macro-hardness of the samples was determined using Rockwell Hardness testing machine (Zwick Roell Group, UK). Each measurement was repeated 4-5 times

Microstructures of the alloys were characterized using a scanning electron microscope and corresponding compositions were analyzed with Energy-dispersive X-ray spectroscopy (EDX).

4.2 Computation details

Calculations were conducted within the first-principles density functional theory (DFT) as implemented in the Vienna ab-initio simulation package (VASP) [37, 47, 48]. DFT is a computational quantum mechanical modelling method used to investigate the electronic structure of many-body systems [49]. Electron interactions were treated with the projector-augmented wave method. The generalized gradient approximation (GGA) of Perdew-Burke-Ernzerhof (PBE) was used for the exchange and correlation effects [50]. The cut-off energy for plane wave basis was set to 400 eV. M_7C_3 is determined by Herbstein and Snyman to be isostructural to Ru_7B_3 with space group P63mc (nr. 186) [51]. A Monkhorst-pack [52] sampling of $7 \times 7 \times 9$ k-point mesh was adopted to achieve self-consistent field convergence, and $11 \times 11 \times 13$ k-point mesh was adopted to compute total energy, charge density and

electronic structure. In all calculations, self-consistency was achieved when the total energy difference between cycles was smaller than 0.1 meV. The geometry relaxation tolerance in all forces was below 0.01 eV/Å. The moduli are calculated by Yu's method [53] as well as Voigt–Reuss–Hill approximation [54]. The alloy matrix is determined to be a bcc structure with 15 Fe atoms and 1 Cr atom according to real Cr concentration in matrix.

4.3 Results and discussion

4.3.1 Microstructure

Fig. 4.1 illustrates typical SEM microstructure images of fabricated alloys with 5%C and different Cr concentrations, 5%, 10%, 20%, 30% and 35%. The alloys show hypereutectic microstructures. The volume fractions of 5%C alloys with different Cr contents were determined by image analysis based on obtained SEM figures. The Cr content did not show a significant influence on the volume fractions of carbides, which were 61%, 65.7%, 56.2%, 57.5%, and 59.6% for samples of 5-5 (Fe-5%Cr-5%C) to 35-5 (Fe-35%Cr-5%C), respectively. Table 4.1 presents concentrations of Cr and Fe in both carbide and ferrous matrix of the HCCIs measured using EDX. As shown, with increasing Cr concentration, the Cr/Fe ratio varies in both carbide and the matrix. However, the overall contents of Cr and Fe in the carbide and matrix (in form of ferrite) keep approximately unchanged. Or in other words, adding Cr changes the Cr/Fe ratio but the total amount of metallic elements (Cr and Fe) for forming M_7C_3 carbides and the matrix are approximately constant, bear in mind that the carbon content is the same for all these HCCIs. This

could be the reason why the carbide volume fraction did not show significant changes when %Cr was varied.

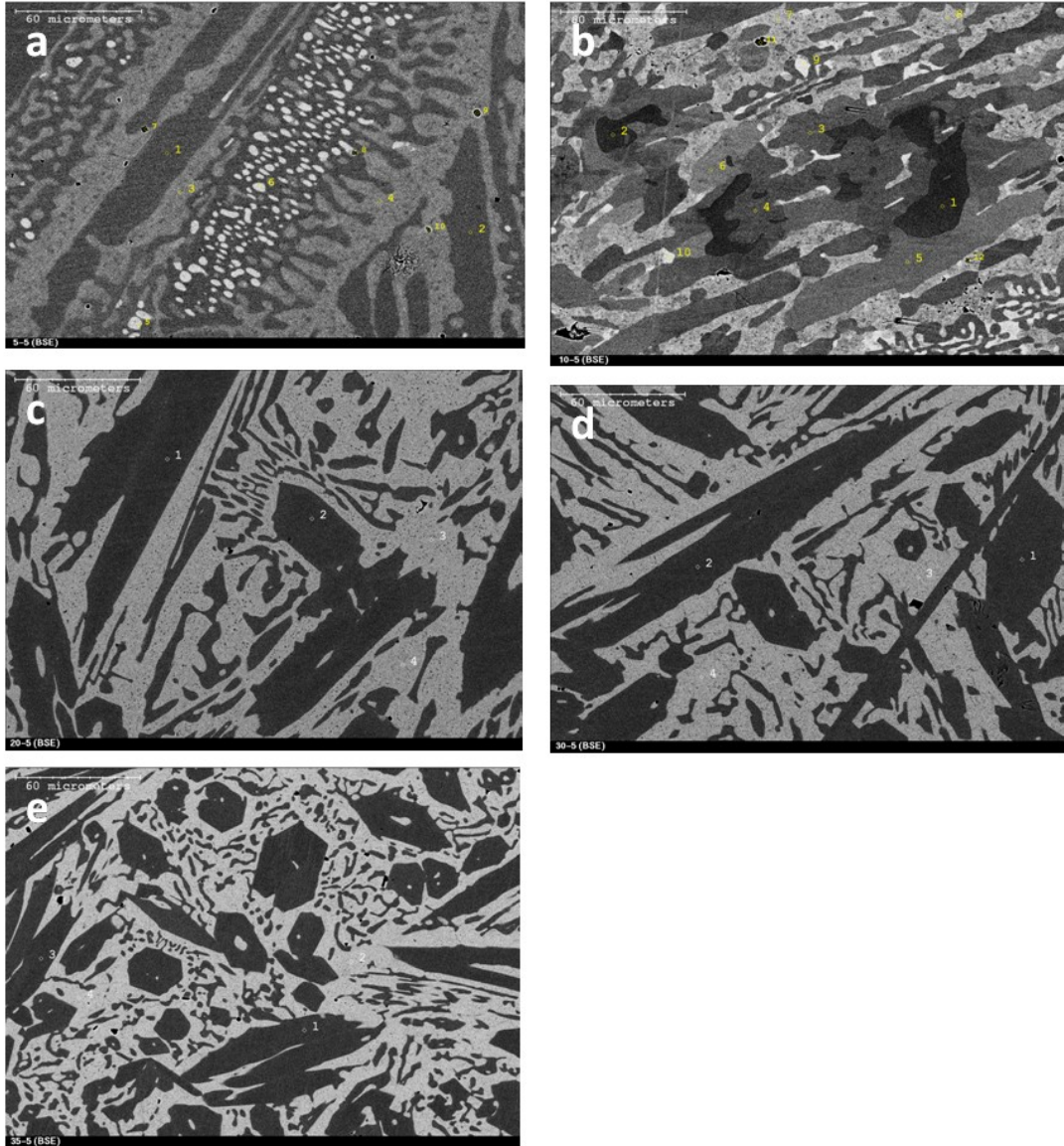


Figure 4.1 Back-scattered electron (BSE) micrographs of microstructures of (a) #5-5, (b) #10-5, (c) #20-5, (d) #30-5, (e) #35-5.

Through examining different areas, a general impression is that alloy #5-5 shows a

slightly finer microstructure and #10-5 has $M_{23}C_6$ solidified around M_7C_3 carbides [55]. Since all these alloys were in the hypereutectic state with their carbide fraction around 60%, difference in their performance during erosion tests as shown later is likely more attributed to variations in compositions of carbides and the matrix in the alloys, especially for 20-5 to 35-5, which have similar microstructures, with primary M_7C_3 carbides embedded in ferrous matrix.

Table 4.1 Measured average values of compositions and Cr/Fe ratios of $(Fe, Cr)_7C_3$ carbide and matrix in the HCCIs determined with EDX.

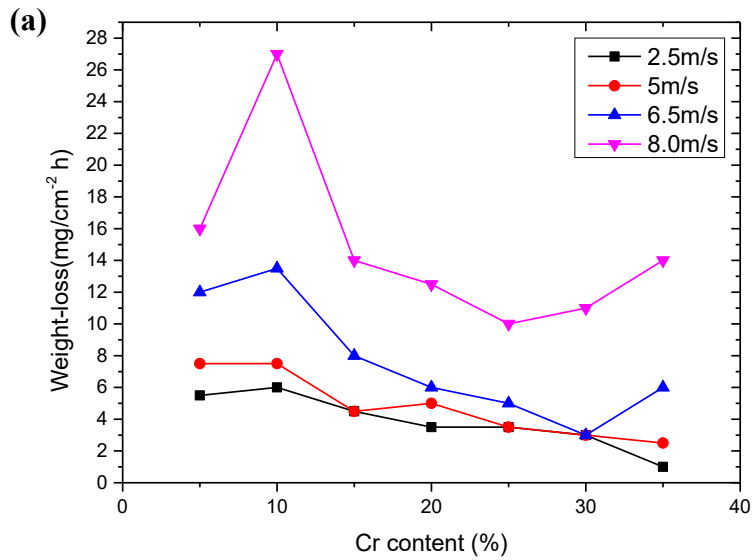
Samples	Carbide				Matrix			
	Cr(at%)	Fe(at%)	Cr+Fe (at%)	Cr/Fe	Cr(at%)	Fe(at%)	Cr+Fe (at%)	Cr/Fe
#5-5	7.04	89.37	96.4	0.08	1.64	93.34	95	0.018
#10-5	21.75	74.95	96.7	0.29	2.75	92.42	95.2	0.030
#20-5	46.51	50.51	97.02	0.92	5.77	90.17	95.9	0.064
#35-5	64.94	32.12	97.06	2.02	11.32	83.34	94.7	0.136

Note: since EDX is unable to detect light elements with meaningful information, data for carbon is not included.

4.3.2 Performance during slurry erosion tests

Fig. 4.2 shows the performance of HCCIs with 5%C but different Cr contents during slurry erosion tests. As shown in Fig. 4.2 (a) for erosion test in a slurry with pH=5, at low slurry velocities i.e. 2.5 m/s and 5 m/s, the material loss decreases as %Cr increases. At higher slurry velocities, the material loss increases due to enhanced mechanical attack with larger wearing forces. In addition, failure of

passive film caused by high-velocity erosion may also contribute to the increase in material loss. A passive film acts as a protective film to reduce corrosion and material loss caused by erosion-corrosion attack. However, when the velocity of slurry flow exceeds a critical value, e.g., about 4 m/s as observed in a study on stainless steel [23, 56], the passive film is damaged and passive film re-growth rate is lower than that for damaging. In this case, the role that the passive film plays in protecting the surface from erosion-corrosion attack is weakened.



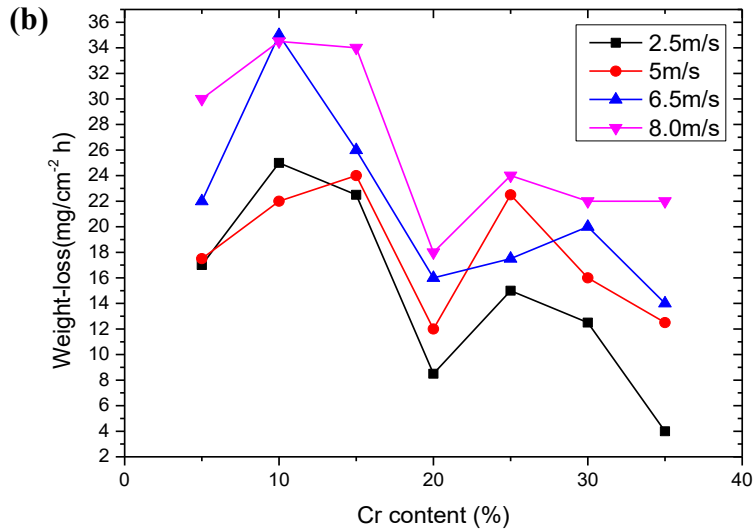


Figure 4.2 Weight-loss mapping of varied chromium iron dependent of chromium concentration at 45°impinging angle in pH=5(a) and pH=3(b), respectively. During the slurry erosion test, a sample travelled over 15 km.

Alloy #10-5 shows the poorest performance. As %Cr increases the material loss decreases and then somewhat increases when %Cr exceeds 25-30%. Such variations should be mainly caused by changes in mechanical properties of the alloys, especially at higher slurry velocities at which the passive film may not play a significant role as a protective layer as mentioned earlier. It was noticed that alloy #5-5 performed better than #10-5 especially at higher velocities (see Fig. 4.2(a)). It should be mentioned that #5-5 did not have sufficient chromium to form an integrated passive film. Thus, its better performance, compared to #10-5, could benefit from its mechanical properties. It is noticed that #10-5 has a fair amount of $M_{23}C_6$, which is softer than M_7C_3 . $M_{23}C_6$ could be responsible for lower wear

resistance of #10-5. The better performance of #5-5 may also benefit from its finer microstructure that helps more effectively block cracking and improve energy dissipation capability especially during erosion at higher slurry velocities. At high slurry velocities, the passive film was damaged and mechanical durability became more important. This could explain why the difference in erosion resistance between #10-5 and #5-5 was even larger when tested at 8 m/s.

Results of tests in the slurry with pH=3 show a trend partially different from that observed during erosion in the slurry with pH5. Again, alloy #10-5 shows the poorest performance. The material loss decreases afterwards, then increases, and finally decreases again after the Cr content exceeds about 25% as Fig. 4.2(b) illustrates. Alloy #5-5 still shows better performance than #10-5. After #10-5, the material becomes better as %Cr increases but continuously increasing %Cr does not show the beneficial effect (after 20%Cr), leading to higher erosion damage. However, in this slurry with lower pH value, there is a second decrease in material loss at higher %Cr, which could be attributed to improved passivation capability when the Cr content is sufficiently increased, especially in the slurry with lower pH and consequently higher corrosivity. The second decrease is smaller at higher slurry velocities, e.g., 8 m/s, since the passivation becomes less important at higher erosion velocities. Before the second decrease, the material loss increases within the range of 20%~30%Cr. This could be more related to variations in the mechanical behavior, as discussed in next sections.

It may need to note that in the slurry of pH3, material loss is generally much more than that in the slurry of pH5. As pH value decreased to 3, the corrosivity of the

acidic slurry considerably increased, which enhanced the erosion-corrosion synergy, leading to larger material loss. It appears that the raised corrosivity somehow minimized the effect of slurry velocity on material removal due to increased involvement of corrosion attack.

4.3.3. Work function, modulus and hardness of $Fe_{7-x}Cr_xC_3$ and matrix

As demonstrated in Fig. 4.2(a), erosion in the slurry of pH5 with lower corrosivity, the mechanical strength should play a main role in resisting erosion, especially at higher slurry velocities. Since the microstructure of the alloys did not significantly change and their volume fractions of carbides are similar, the observed variations in the erosion resistance of the alloys may largely result from possible variations in mechanical strength of alloys due to changes in Cr content in carbide, $(Fe,Cr)_7C_3$, and in the matrix as well.

In order to understand the performance of the alloys and the role that Cr plays, we analyzed compositions, Young's moduli, hardness values and corresponding electron work functions of $(Fe,Cr)_7C_3$ carbide and matrix for four alloys: #5-5, #10-5, #20-5 and #35-5, using EDX, micro-indenter, and Peakforce KPFM which was used to determine Young's modulus and electron work function, respectively. In order to facilitate mapping electron work function and modulus, carbide and the ferrous matrix were distinguished with the magnetic force microscopy (MFM) using a Bruker magnetic probes (MESP), since the ferrous matrix and carbide have

different magnetic properties. Fig 4.3 illustrates a representative MFM image and corresponding maps of work function and reduced Young's modulus in the same area. The ferrous matrix has a striped appearance in Fig 4.3(a) due to its ferromagnetic behavior, while the carbide (paramagnetic) shows a uniform appearance. The purpose of in situ mapping both work function and modulus is to view the relation between modulus and work function. As illustrated, EWF and modulus are closely correlated. The higher the EWF, the larger is the modulus. The carbide (lighter color) has higher work function and greater modulus than the matrix (darker).

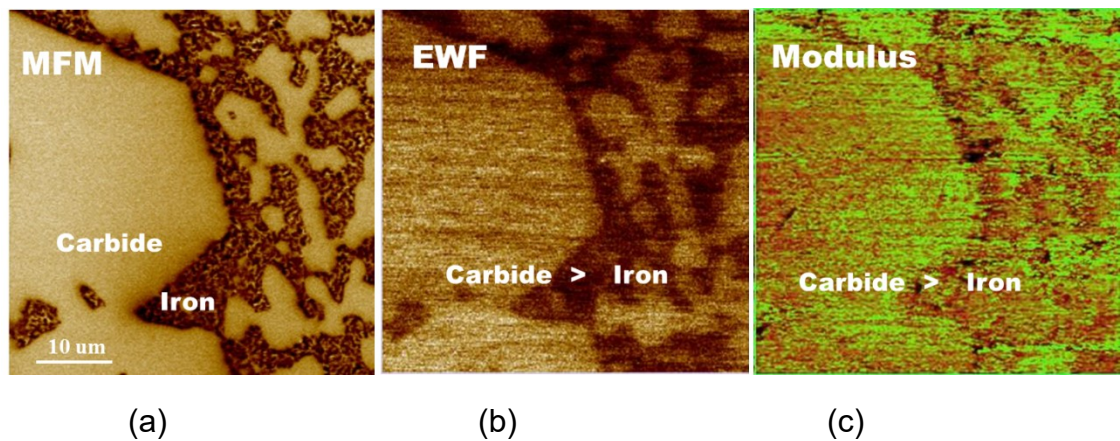


Figure 4.3 (a) A MFM image of a #20-5 HCCI, (b) corresponding work function map, and (c) corresponding modulus map (zones in green have higher modulus).

For more precise information on mechanical properties, a micro-indenter was used to measure micro-hardness and Young's modulus for carbides and matrix in the HCCIs. Modulus of #10-5 was measured in the central area of the carbide (M_7C_3). Results of the micro-indentation measurements are presented in Fig. 4.4. One may see that the modulus of carbide and corresponding work function increase until

reach the level of Cr at 20%, and then decrease as Figs. 4.4 (a) and (b) illustrate. However, both the modulus and work function of the matrix increase with the increase in %Cr. In Fig. 4.4 (c) and (d), micro-hardness and macro-hardness are presented respectively, which show similar trends with the Cr content, indicating that carbide's hardness has larger effect on HCCI than matrix. It seems sample #20-5, with Cr/Fe ratio of 0.92 in carbide (see Table 4.1) has the strongest mechanical properties. The hardness of matrix keeps at a similar level until sample #35-5, but the variation is minor.

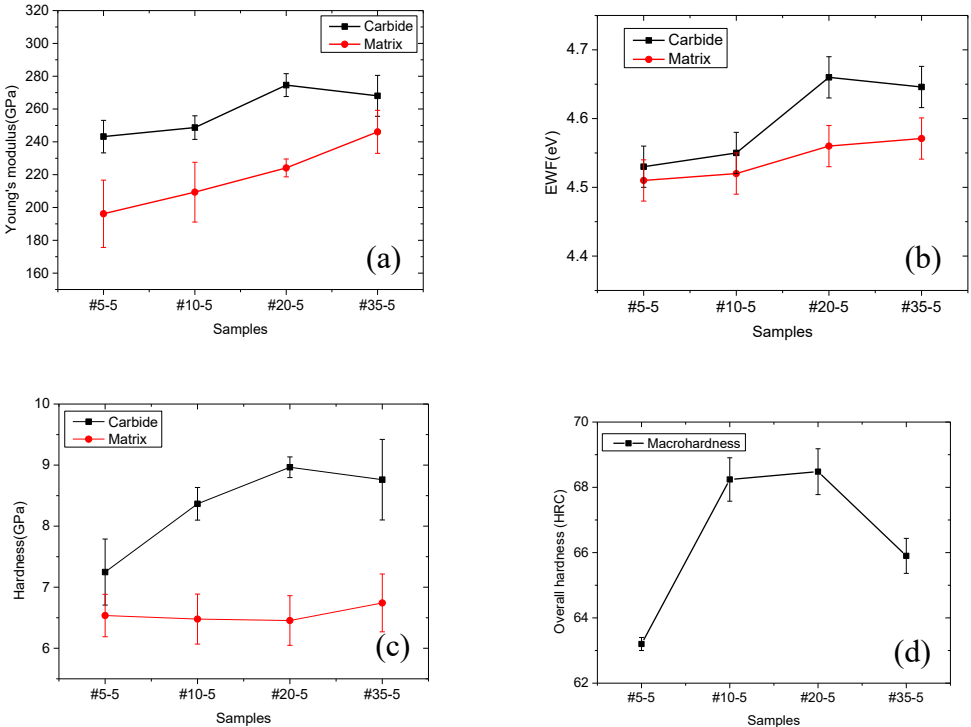


Figure 4.4 The experimentally measured (a) modulus and (b) work function (c) microhardness of carbides and matrix and (d) Macro-hardness of samples at different Cr content levels.

As demonstrated previously [57, 58], Young's modulus of metals and alloys vary with work function in a sixth power relationship, i.e., the higher the work function, the greater the modulus. Such a trend exists for the matrix as shown in Figs. 4.4 (a) and (b). However, previously whether such a relationship was applicable to carbides was unknown. The current measurement shows that this relationship also works for carbides as Figs. 4.4(a) and (b) illustrate. In order to understand underlying mechanisms, first-principles calculation was conducted to investigate how carbide's mechanical strength varies with the Cr/Fe ratio and correlate the variation with the electron density, which is related work function in Chapter 5.

4.4 First-Principles Calculation

4.4.1 Mechanical properties of carbides

The first-principles method was applied to calculation bulk modulus(B), shear modulus(G) and Young's modulus(E) of $Fe_{7-x}Cr_xC_3$, results of which are showed in Fig. 4.5(a). Since only integer numbers of Cr atoms can be added, six Cr/Fe ratios were analyzed. All moduli of $Fe_6Cr_1C_3$ are lower than those of Fe_7C_3 , indicating that adding minor Cr may lower carbide's mechanical strength. As more Cr atoms are doped in carbide, bulk modulus increase until reach maximum at Cr_7C_3 while shear and Young's moduli increase and reach a maximum at $Fe_3Cr_4C_3$ and then decrease when the Cr/Fe ratio continuously increases. This trend is consistent with calculation in CASTEP by Zhang, et al [1], which shows $Fe_4Cr_3C_6$ has the maximum G and E, although their calculation does not show decreased moduli for $Fe_6Cr_1C_3$. Thus, the calculation in this study is proved to be effective.

The hardness of carbides has also been calculated based on the shear modulus and Pugh's ratio($k=G/B$) [59]. An empirical equation proposed by Chen [60], which performs well across a wide range of hardness values and is proved effective for various materials was employed to calculate the carbides' hardness.

$$H_v(\text{GPa})=2(k^2G)^{0.585}-3 \quad (4.1)$$

Hardness values calculated using this equation are shown in Fig. 4.5(b). Although $\text{Fe}_3\text{Cr}_4\text{C}_3$ has the highest shear modulus and Young's modulus, its hardness is smaller than $\text{Fe}_4\text{Cr}_3\text{C}_3$, since Pugh's ratio plays an important role in Eq. 4.1. The trend of variation in calculated hardness is consistent with experiment data shown in Fig. 4.4(c), although the values are not exactly the same. With 3 or 4 Cr atoms doped, the Cr/Fe ratio is 3/4 or 4/3, both of which are close to 1. Corresponding carbides show superior mechanical properties (Fig. 4.4(c)) and performance (Fig. 4.2). This is consistent the performance of sample #20-5(see Table 4.1), whose Cr/Fe ratio is 0.92 by EDX analysis.

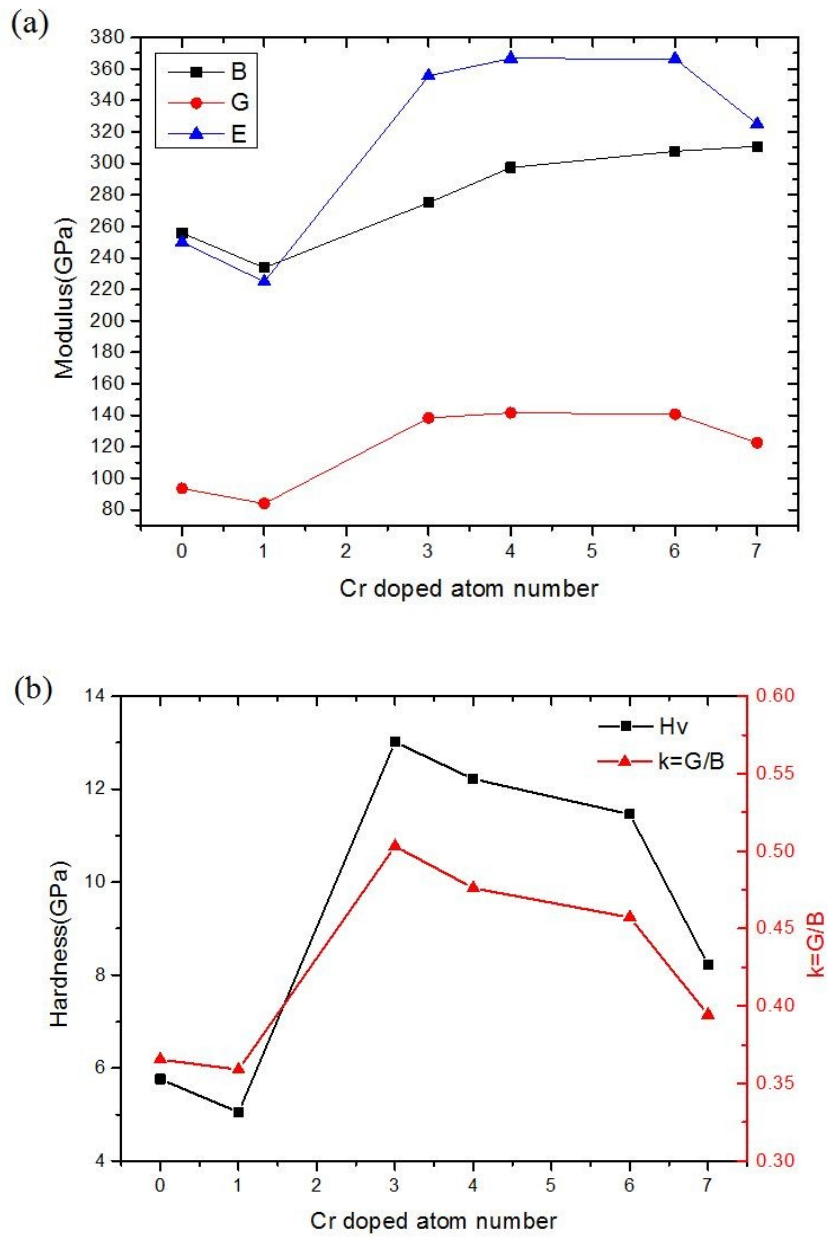


Figure 4.5 (a) Bulk modulus(B), shear modulus(G) and Young's modulus(E) of samples; (b) The hardness Hv calculated by Eq. (4.1).

4.4.2 Potential and charge density of the ferrous matrix

As shown in Fig. 4.4, alloyed Cr increased modulus and work function of the matrix. In order to better understand the observed phenomena, effects of Cr atoms on potential and electron density of the ferrous matrix were analyzed. Fig. 4.6(a) illustrates a 15Fe-1Cr cell, for which the potential and electron density are analyzed. Fig. 4.6(b) and Fig. 4.7(c) show the potential and electron density of (110) plane of the Cr-doped iron cell, respectively. As demonstrated, the potential between adjacent Fe and Cr atoms is lower, accompanied with higher electron density, than that between adjacent Fe and Fe atoms. This is an indication that adding Cr increases the work function and makes the atomic bond stronger. Thus, if exposed to air, the Cr-containing material with its surface energy higher than that of pure iron is easier to react and form a passive layer, which protects the material from corrosion. Thus, we may conclude that adding Cr does not only mechanically strengthen the material but also enhances its corrosion resistance.

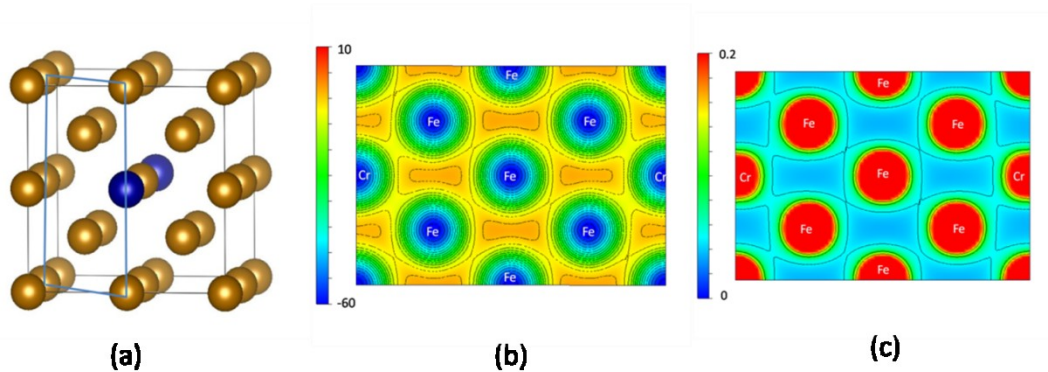


Figure 4.6 (a) a BCC structured 15Fe (golden)-1Cr (blue) alloy cell, (b) a local potential plot of (110) plane, and (c) an electron density plot of (110) plane.

4.5 Understanding of the overall performance

With measured local moduli and work functions of carbide and matrix as well as the computational analysis using the first-principles method, the overall performance of the HCCIs can be explained, and the extracted information or clues would be helpful for modification of HCCIs.

As shown in Fig. 4.2(a), erosion decreases as %Cr increases. This is attributed to the strengthening effect of Cr on both carbide and the matrix. However, when the %Cr is high enough, its benefit to carbide is lowered as Figs. 4.4 and 4.5 illustrate, leading to somewhat increase in material loss during the erosion tests, especially at higher slurry velocities (see Fig. 4.2(a)).

It was observed that #5-5 alloy performed better than #10-5. As noticed, #10-5 has a fair amount of softer $M_{23}C_6$. Thus, the better performance of #5-5, compared to #10-5, is likely ascribed to its finer microstructure (see Fig. 4.1) that may help block cracking more effectively during erosion processes especially at higher slurry velocities, and lowered hardness of carbides.

When tested in the slurry (pH3) with higher corrosivity, the alloys show a trend similar to that obtained at pH5 but the material loss decreases after 25%Cr as Fig. 4.2(b) illustrates. Such a decrease in material loss should result from the higher %Cr in the matrix, which helped suppress erosion-corrosion synergy and thus material loss. Such a decrease in material loss was not observed when testing was performed in the slurry of pH5 with lower corrosivity.

4.6 Summary

Through slurry erosion test of HCCIs containing 5%C and 5~35%Cr and measurement of their local moduli and work functions of carbide and matrix as well as the computational analysis using the first-principles method, their mechanical properties and erosion-corrosion performance are studied. The following conclusions are drawn from this study:

- 1) As Cr/Fe ratio increases, the strength of carbide, $(Fe, Cr)_7C_3$, in high-Cr cast irons initially increases, reaching the maximum at about $Cr/Fe \approx 4/3$, and then decreases as Cr/Fe continuously increases.
- 2) The strength of the ferrous matrix increases with an increase in the content of alloyed Cr.
- 3) The higher the electron work function, the higher the mechanical strength and stability. This relationship is applicable to both the metallic matrix and $(Fe, Cr)_7C_3$ carbide.
- 4) In the slurry with lower corrosivity (pH5), increasing %Cr of the HCCIs enhances their overall resistance to erosion. However, the situation is reversed when %Cr is sufficiently high, ascribed to the decrease in strength of the carbide when its Cr/Fe ratio exceeds a certain level. This is more visible at higher slurry velocities.
- 5) In the slurry with high corrosivity (pH3), material loss decreases at high %Cr, which should be attributed to the improvement in passivation, which helps suppress erosion-corrosion synergy and thus reduce the overall material loss.
- 6) #10-5 showed poorest performance, which could be attributed to the existence of a large fraction of softer $M_{23}C_6$ carbides.

5 Further studies on the correlation between electronic and mechanical properties of $(\text{Fe}, \text{Cr})_7\text{C}_3$ carbides

5.1 Carbides Young's modulus VS Electron work function

In Chapter 4, we measured both Young modulus and work function for carbides and matrix. The results of $(\text{Fe}, \text{Cr})_7\text{C}_3$ carbides of four samples are shown in Fig. 5.1.

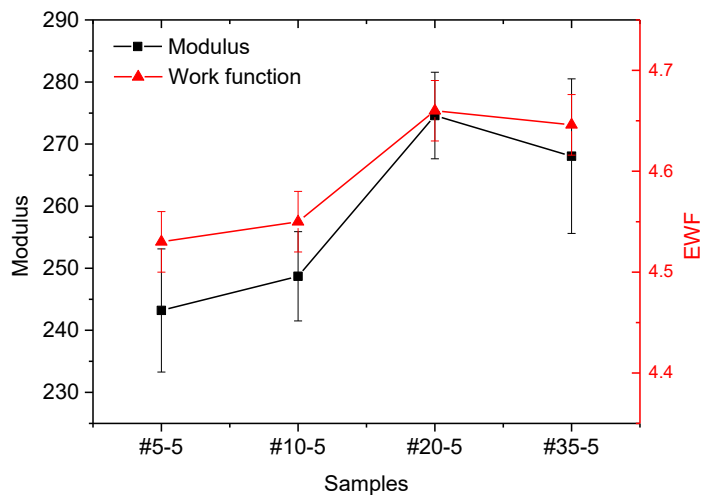


Figure 5.1 Measured work function and Young's modulus of carbides in samples #5-5, #10-5, #20-5 and #35-5.

One may see that the electron work function and corresponding modulus of $(\text{Fe}, \text{Cr})_7\text{C}_3$ carbides initially increase and then decrease after reaching the maximum as

the Cr/Fe ratio increases. Two main phenomena are observed. First, the properties of M_7C_3 are influenced by the Cr/Fe ratio. Second, the trend of variations in EWF is similar to that of modulus. Such consistency in work function and Young's modulus has already been proved for metals and alloys in previous papers [57, 58]. In order to understand the observation that such a relation between Young's modulus and work function is also applicable to the carbide, further first-principles analysis on bonds was conducted to investigate how carbide's mechanical strength varies with the Cr/Fe ratio and corresponding electron density, which is related with work function. Detailed results are given in this chapter.

5.2 Results and discussion

5.2.1 Structure and formation energy

Fig. 5.2 illustrates atomic arrangement of M_7C_3 carbide [51], with which the system energy, electronic configuration and properties were analyzed and calculated.

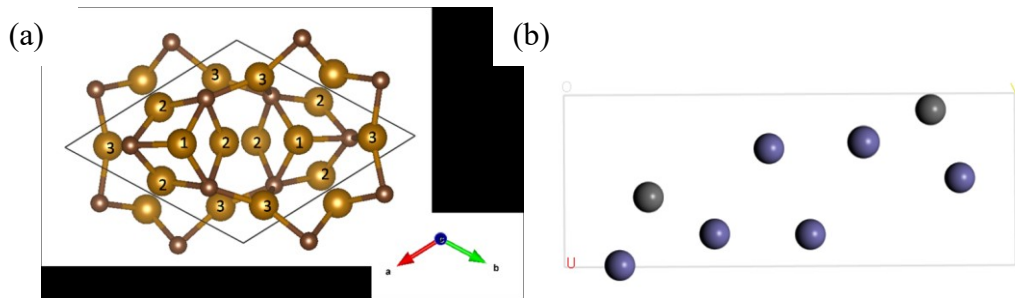


Figure 5.2 (a) Atomic structure of M_7C_3 carbide. (large: metal; small: carbon) (b) (110) plane configuration of M_7C_3 carbide. (purple: metal; grey: carbon)

The formation enthalpy (ΔH) can be calculated:

$$\Delta H = H(\text{Fe}_x\text{Cr}_y\text{C}_z) - [xH(\text{Fe}) + yH(\text{Cr}) + zH(\text{C})] \quad (5.1)$$

Where x, y, z are number of Fe, Cr, and C atoms in the carbides, respectively. At T=0K and p=0 Pa, the formation energy is equal to formation enthalpy. The formation energies of (Fe, Cr)₇C₃ carbides with different Fe/Cr ratios are calculated by subtracting energies of Fe, Cr and C from calculated carbide's energy. Results of the calculations are listed in Table 5.1.

Table 5.1 Calculated coordinates of atoms and formation energy of (Fe, Cr)₇C₃.

Formula	Sites position	Formation energy ΔH (ev/unit)	Metal atom	x/a, y/b, z/c
Fe ₇ C ₃	Fe: 1,2,3	0.0944	Position 1: 2b	1/3, 2/3, 0.4022
Fe ₆ Cr ₁ C ₃	Fe: 2,3 Cr: 1	-0.1384		
Fe ₄ Cr ₃ C ₃	Fe: 1,3 Cr: 2	-1.6172	Position 2: 6c	0.5456, 0.4544, 0.4089
Fe ₃ Cr ₄ C ₃	Fe: 2 Cr:1,3	-2.1833		
Fe ₁ Cr ₆ C ₃	Fe: 1 Cr:2,3	-2.7178	Position 3: 6c	0.1225, 0.8775, 0.5833
Cr ₇ C ₃	Cr: 1,2,3	-3.5331		

Corresponding atomic configurations of the (Fe, Cr)₇C₃ carbides are also given in Table 5.1. As shown, the formation energy of Cr₇C₃ is the lowest, meaning that Cr₇C₃ is most stable among all carbides and adding Cr helps form carbides in cast irons.

5.2.2 Density of states (DOS) and Bader charge analysis

It has been demonstrated in previous papers that the bonds of M_7C_3 possess both covalent and ionic characters [1, 61, 62]. Music's work in 2004 shows a covalent-ionic Cr-C-Cr chain immersed in a Fermi electron gas in orthorhombic Cr_7C_3 carbide [62], which is consistent with the work in this paper. The covalent bond is usually formed from two electrons, one from each atom participating in the bond. The electrons forming the bond tend to be partly localized in the region between the two atoms joined in the bond and their spins in the bond tend to be antiparallel [63]. Thus, the electron density between two atoms forming covalent bond would be relatively high. In Fig. 5.3, C band has overlapped peak with Fe band and Cr band near -5eV , while not totally overlapped above -3eV . Thus electrons from C and metal atom having the same energy state form the covalent bond in M_7C_3 carbide.

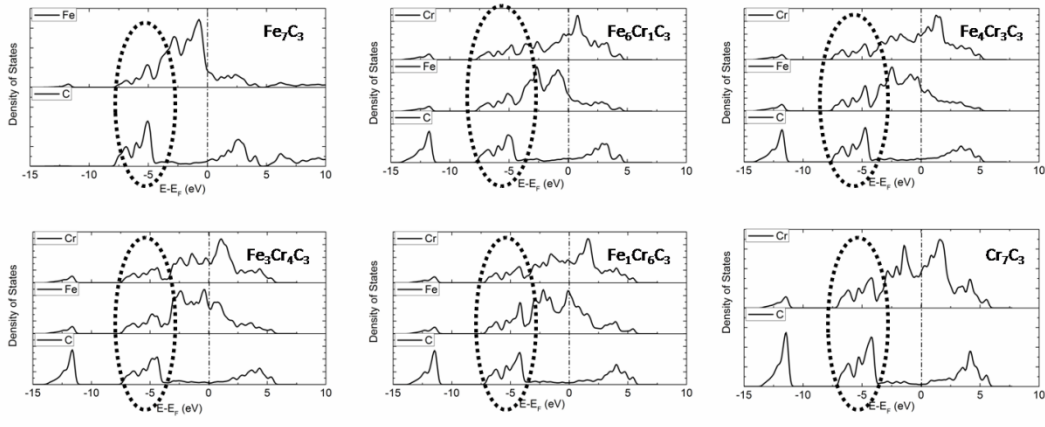


Figure 5.3 Atom-projected densities of states for bulk $Fe_{7-x}Cr_xC_3$ carbide systems. For each system, band overlap of metal and carbon near -5eV are responsible for covalent bond between metal-carbon.

We also did Bader charge analysis [64] on $(\text{Fe}, \text{Cr})_7\text{C}_3$ carbides to prove ionic character between C and metal element, results of which are shown in Table 5.2. If electrons transfer from one atom to another to form positive and negative ions, these two ions would attract each other due to Coulombic force and such attraction will form ionic bond. Thus, if more electrons transfer, the ionic character would be more obvious and the ionic bond would be stronger. Thus, the electron density cloud of those two ions tend to be one larger and the other smaller. As shown in Table 5.2, as Cr atoms increases, the number of electrons that each C atom receives from metal atoms increases, from 1 electron in Fe_7C_3 to 1.47 electrons in Cr_7C_3 . Thus we may conclude that C-Cr bonding is more ionic than C-Fe bonding, which is consistent with the electron density distribution in Fig. 5.4 and electronegativity of Fe (=1.83) and Cr (=1.66), since ionic bond is more likely to form between two elements with quite different electronegativities.

Table 5.2 Bader charge transfers from metal to carbon atoms (e/atom). Values positive mean lose electron and negative mean get electron.

	Fe_7C_3	$\text{Fe}_6\text{Cr}_1\text{C}_3$	$\text{Fe}_4\text{Cr}_3\text{C}_3$	$\text{Fe}_3\text{Cr}_4\text{C}_3$	$\text{Fe}_1\text{Cr}_6\text{C}_3$	Cr_7C_3
Fe	+0.43	+0.38	+0.35	+0.24	+0.16	/
Cr	/	+0.81	+0.71	+0.78	+0.66	+0.63
C	-1	-1.06	-1.17	-1.28	-1.38	-1.47

The energy of 0eV is fermi energy, below which the states are occupied by electrons. Thus, as the number of Cr atoms increases (Fig. 5.3), the energy states occupied by electrons decreases, and more states of the metal is vacant. Those states of metal at

high energy are antibonding states, the filling of which would reduce the bond strength [65]. In Cr_7C_3 , the antibonding states are partly filled while in Fe_7C_3 , they are almost totally filled, implying that Fe-Fe bonding strength is not as strong as Cr-Cr bond. Thus, doping Cr atoms may enhance the metal-metal interaction, which is consistent with the variation in electron density as Fig. 5.4 illustrates.

5.2.3 Electron density (e/angstrom³)

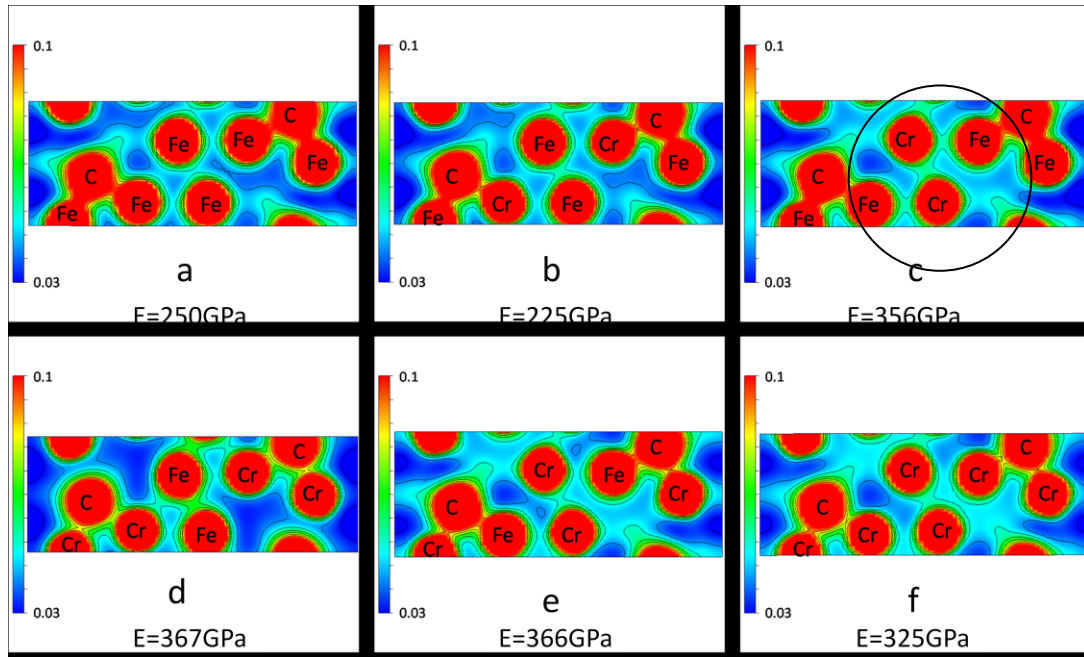


Figure 5.4 Electron density distribution of the (110) plane of Fe_7C_3 (a), $\text{Fe}_6\text{Cr}_1\text{C}_3$ (b), $\text{Fe}_4\text{Cr}_3\text{C}_3$ (c), $\text{Fe}_3\text{Cr}_4\text{C}_3$ (d), $\text{Fe}_1\text{Cr}_6\text{C}_3$ (e) and Cr_7C_3 (f). For each system, minimum, maximum and isoline values are set the same. Electron densities between metal-metal atoms are most pronounced in c) and d), and are responsible for their high Young's modulus.

Fig. 5.4 shows electron density distribution of (110) plane of $(\text{Fe}, \text{Cr})_7\text{C}_3$ with different Cr contents respectively. In section 5.2.2, we have proved that the bond between C and metal has both covalent and ionic character, which make the bond stable and strong. These characters are also manifested in electron density distribution and more details are given. In Fig. 5.4b, by comparing C-Fe bond and C-Cr bond, it is obvious that electron density between C-Fe is higher than that between C-Cr, indicating that C-Fe could be more covalent than C-Cr. From Fig. 5.4a to Fig. 5.4f, one may also see the increase of electron density in interstitial places between atoms. Those electrons are less localized, which may contribute to metallicity of the material and act as glue between atoms when concerning mechanical strength. Thus, it may be concluded that as Cr content increases, the carbide's metallicity increases. Music's work in 2004 shows a Cr-C-Cr chain immersed in a Fermi electron gas in orthorhombic Cr_7C_3 carbide [62]. Metal-carbon-metal chains shown in Figs. 5.4a-f are consistent with his research. In Fig. 5.4c and Fig. 5.4d, the higher electron density between metal atoms in the circle area helps form longer electron chains immersed in Fermi electron gas, which could be responsible for their higher Young's modulus and shear modulus as shown in Chapter 4. Since metallic bond strength is dependent on electron density, which can be reflected by work function [58], a higher electron density between metal atoms corresponds to higher work function and stronger metallic bonds.

5.2.4 Further discussion on mechanism

According to the first-principles analysis of covalent and ionic characters of $(\text{Fe}, \text{Cr})_7\text{C}_3$ carbides with respect to the Cr content, as the Cr content increases in $(\text{Fe},$

$(\text{Cr})_7\text{C}_3$ carbide, the covalency of carbon-metal bond decreases while its ionicity increases. Since metallic bond is generally weaker than covalent and ionic bonds due to its random distribution and less localization of electrons, when the carbide is damaged, the weakest point is broken down first. Thus, structure's mechanical properties are mainly dependent on the weakest bonding. This is also shown in other systems, such as that shown in Zhang's research on rhenium nitrides, which demonstrates that weak “ionic” Re-N bonds limit their achievable strength and are also responsible for their unusual mechanical properties [66]. In this study, as Fig. 5.4 illustrates, the mechanical strength of the carbide is dependent on the metal-metal bonds in the circle area, which will affect the Young's modulus of $(\text{Fe}, \text{Cr})_7\text{C}_3$ and shear modulus, and metal-metal bonds have positive relation with work function. Thus, for M_7C_3 carbides, work function will have positive relation with their mechanical strength.

5.3 Summary

1. It was demonstrated that the electron work function and corresponding modulus of $(\text{Fe}, \text{Cr})_7\text{C}_3$ carbides initially increase and then decrease after reaching the maximum as the Cr/Fe ratio increases, which is consistent with calculation result that $\text{Fe}_4\text{Cr}_3\text{C}_3$ carbide shows largest elastic modulus.
2. By computational analysis on bonds of M_7C_3 carbides, we learned the importance of metal-metal interaction in M_7C_3 carbides. These metal-metal bonds connects small metal-carbon-metal units and help form longer chains, which is beneficial to carbides strength. Thus, the metal-metal bonds play a predominant role in

determining the mechanical strength of M_7C_3 carbides.

3. As demonstrated previously, Young's modulus of metals and alloys increases as work function increases in a sixth power relationship [57, 58], work function might be positive related with metallic electron density, and that's why measured work function has a positive relationship with Young's modulus of M_7C_3 carbides.

6 General Conclusions and Future Work

6.1 General conclusions of the research

This work focuses on HCCIs' carbides, which are very important components for their wear resistance. Morphology and composition are two aspects that we investigated by different methods respectively, and their correlations with HCCIs' performance are discussed. Besides, via theoretical calculation, the consistency between carbides' work function and mechanical properties is analyzed.

1. Through MSDM modeling, the core-shell structured carbides in hypereutectic HCCI are proved to be effective in minimizing the stress at the carbide/matrix interface, thus lowering the probability of interfacial failure. However, if the shell is too thick, it will deteriorate the whole carbide's hardness and thus the HCCIs' erosion resistance. It is demonstrated that elongated carbides aligned in the particle impingement direction perform better than those which are perpendicular to the impingement direction.

2. The overall erosion- corrosion performance of HCCI with 5% C and 5-35% and their mechanical properties are discussed. It is demonstrated that as Cr/Fe ratio increases, the strength of carbide, $(\text{Fe}, \text{Cr})_7\text{C}_3$, in high-Cr cast irons initially increases, reaching the maximum at about $\text{Cr}/\text{Fe} \approx 4/3$, and then decreases as Cr/Fe continuously increases, while that of the ferrous matrix increases. Besides, it is demonstrated that EWF and $(\text{Fe}, \text{Cr})_7\text{C}_3$ carbides' mechanical properties has the

same trend as Cr/Fe ratio varies.

3. Through first-principles calculation of $(\text{Fe}, \text{Cr})_7\text{C}_3$ carbides with different Cr atom numbers doped, it is demonstrated that $(\text{Fe}, \text{Cr})_7\text{C}_3$ carbides is composed of metal-carbon-metal chains immersed in a Fermi electron gas. The metal-metal bonds connects these small chains, thus are fundamental for the material's mechanical strength.

4. The metallic bond strength is dependent on electron density, which is related with work function. Since $(\text{Fe}, \text{Cr})_7\text{C}_3$ carbides' mechanical strength is dominated by the metal-metal bonds, the changes in the strength of $(\text{Fe}, \text{Cr})_7\text{C}_3$ carbide are consistent with changes in their work functions.

6.2 Future work

6.2.1 Extend MSDM to 3-dimensional calculation

The MSDM model for the present study is two dimensional, which does not well reflect real situations. Owing to rapid development of computer technology, it is doable to extend MSDM to three dimensional wear modeling, with incorporation of other tools such as OpenGL, a visualization tool.

6.2.2 Interfacial bonding strength

Currently in MSDM, interfacial bonding strength is not concerned. This is not accurate for multiphase materials. Thus, molecular dynamics and first-principles

calculations can be incorporated to provide the information on the interfacial bonding strength. This would make prediction and analysis more accurate and capable to handle realistic complex systems.

Bibliography

1. Zhang, P., et al., *Optimization on mechanical properties of Fe 7– xCrxC 3 carbides by first-principles investigation*. Journal of Alloys and Compounds, 2013. **560**: p. 49-53.
2. Davis, J.R., K. Mills, and S. Lampman, *Metals handbook. Vol. 1. Properties and selection: Irons, steels, and high-performance alloys*. ASM International, Materials Park, Ohio 44073, USA, 1990. 1063, 1990.
3. Wiengmoon, A., *Carbides in High Chromium Cast Irons*. Naresuan University Engineering Journal, 2011. **6**(1): p. 64.
4. Pearce, J. and D.W. Elwell, *Duplex nature of eutectic carbides in heat treated 30% chromium cast iron*. Journal of materials science letters, 1986. **5**(10): p. 1063-1064.
5. Zumelzu, E., et al., *Microstructural characteristics and corrosion behaviour of high-chromium cast iron alloys in sugar media*. Protection of metals, 2003. **39**(2): p. 183-188.
6. Llewellyn, R., S. Yick, and K. Dolman, *Scouring erosion resistance of metallic materials used in slurry pump service*. Wear, 2004. **256**(6): p. 592-599.
7. Tang, X., et al., *Microstructure of high (45wt.%) chromium cast irons and their resistances to wear and corrosion*. Wear, 2011. **271**(9): p. 1426-1431.
8. Wiengmoon, A., et al., *Microstructural and crystallographical study of carbides in 30wt.% Cr cast irons*. Acta Materialia, 2005. **53**(15): p. 4143-4154.
9. Wiengmoon, A., T. Chairuang Sri, and J.T.H. Pearce, *A microstructural study of destabilised 30wt% Cr-2.3 wt% C high chromium cast iron*. ISIJ international, 2004. **44**(2): p. 396-403.
10. Laird, G., R. Gundlach, and K. Rohrig, *Abrasion-resistant cast iron handbook 2000*: American Foundry Society Illinois.
11. Tang, X., et al., *Beneficial Effects of the Core–Shell Structure of Primary Carbides in High-Cr (45 wt%) White Cast Irons on Their Mechanical Behavior and Wear Resistance*. Tribology Letters, 2015. **58**(3): p. 1-10.
12. Finnie, I. *The mechanism of erosion of ductile metals*. in *3rd US national congress of applied mechanics*. 1958.

13. Shimizu, K., et al., *FEM analysis of erosive wear*. International Journal of Cast Metals Research(UK), 1998. **11**(6): p. 515-520.
14. Shimizu, K., et al., *FEM analysis of the dependency on impact angle during erosive wear*. Wear, 1999. **233**: p. 157-159.
15. Balu, P., et al., *Finite element modeling of solid particle erosion in AISI 4140 steel and nickel-tungsten carbide composite material produced by the laser-based powder deposition process*. Tribology International, 2013. **62**: p. 18-28.
16. Wang, Y.F. and Z.G. Yang, *A coupled finite element and meshfree analysis of erosive wear*. Tribology International, 2009. **42**(2): p. 373-377.
17. Gumbsch, P. and R.M. Cannon, *Atomistic aspects of brittle fracture*. Mrs Bulletin, 2000. **25**(05): p. 15-20.
18. Zhong, W. and D. Tomanek, *First-principles theory of atomic-scale friction*. Physical review letters, 1990. **64**(25): p. 3054.
19. Li, D., et al., *A microscale dynamical model for wear simulation*. Wear, 1999. **225**: p. 380-386.
20. Chen, Q. and D. Li, *Computer simulation of solid-particle erosion of composite materials*. Wear, 2003. **255**(1): p. 78-84.
21. Ouyang, C., S. Zhu, and D. Li, *Experimental and Simulation Studies on the Solid-Particle Erosion of WC-MgO Composites*. Tribology Letters, 2013. **52**(3): p. 501-510.
22. Elalem, K. and D. Li, *Dynamical simulation of an abrasive wear process*. Journal of computer-aided materials design, 1999. **6**(2-3): p. 185-193.
23. Li, L. and D. Li, *Simulation of corrosion-erosion of passive metals using a micro-scale dynamical model*. Wear, 2011. **271**(9): p. 1404-1410.
24. Chen, Q. and D. Li, *Computer simulation of solid particle erosion*. Wear, 2003. **254**(3): p. 203-210.
25. Li, L. and D. Li, *Understanding the influence of microstructure features on the erosion resistance of low-carbon pipeline steel through computational simulation*. Wear, 2013. **301**(1): p. 70-75.
26. Born, M. and J.R. Oppenheimer, *On the quantum theory of molecules*. Сборник статей к мультимедийному электронному учебно-методическому комплексу по дисциплине «физика атома и атомных явлений»/отв. ред. Шундалов МБ; БГУ, Физический факультет, 1927.
27. Lee, J.G., *Computational materials science: an introduction* 2016: Crc Press.

28. Gross, E.K. and R.M. Dreizler, *Density functional theory*. Vol. 337. 2013: Springer Science & Business Media.
29. Schrödinger, E., *Quantization as an eigenvalue problem*. *Annalen der Physik*, 1926. **79**(4): p. 361-376.
30. Born, M., *Quantum mechanics in impact processes*. *Z. Phys*, 1926. **38**: p. 803-827.
31. Jost, R. and A. Pais, *On the scattering of a particle by a static potential*. *Physical review*, 1951. **82**(6): p. 840.
32. Hartree, D.R. *The wave mechanics of an atom with a non-Coulomb central field. Part I. Theory and methods*. in *Mathematical Proceedings of the Cambridge Philosophical Society*. 1928. Cambridge Univ Press.
33. Fock, V., *Approximation method for the solution of the quantum mechanical multibody problems*. *Zeitschrift für Physik*, 1930. **61**: p. 126-148.
34. Hohenberg, P. and W. Kohn, *Inhomogeneous electron gas*. *Physical review*, 1964. **136**(3B): p. B864.
35. Kohn, W. and L.J. Sham, *Self-consistent equations including exchange and correlation effects*. *Physical review*, 1965. **140**(4A): p. A1133.
36. Blöchl, P.E., *Projector augmented-wave method*. *Physical Review B*, 1994. **50**(24): p. 17953.
37. Kresse, G. and D. Joubert, *From ultrasoft pseudopotentials to the projector augmented-wave method*. *Physical Review B*, 1999. **59**(3): p. 1758.
38. Karantzalis, A., A. Lekatou, and H. Mavros, *Microstructural modifications of as-cast high-chromium white iron by heat treatment*. *Journal of materials engineering and performance*, 2009. **18**(2): p. 174-181.
39. Gao, X., et al., *Effect of thermomechanical treatment on sliding wear of high-Cr cast iron with large plastic deformation*. *Tribology International*, 2015. **92**: p. 117-125.
40. Coronado, J., *Effect of load and carbide orientation on abrasive wear resistance of white cast iron*. *Wear*, 2011. **270**(11): p. 823-827.
41. Chung, R.J., *Comprehensive study of the abrasive wear and slurry erosion behavior of an expanded system of high chromium cast iron and microstructural modification for enhanced wear resistance*, 2014, University of Alberta.
42. Xiao, B., et al., *Mechanical properties and chemical bonding characteristics of Cr₇C₃ type multicomponent carbides*. *Journal of Applied Physics*, 2011. **109**(2): p. 023507.

43. Lu, H., X. Huang, and D. Li, *Understanding the bond-energy, hardness, and adhesive force from the phase diagram via the electron work function*. Journal of Applied Physics, 2014. **116**(17): p. 173506.
44. Huang, X.C., H. Lu, and D.Y. Li, *Understanding the corrosion behavior of isomorphous Cu–Ni alloy from its electron work function*. Materials Chemistry and Physics, 2016. **173**: p. 238-245.
45. Yu, B., D. Li, and A. Grondin, *Effects of the dissolved oxygen and slurry velocity on erosion–corrosion of carbon steel in aqueous slurries with carbon dioxide and silica sand*. Wear, 2013. **302**(1): p. 1609-1614.
46. Derjaguin BV, M.V., Toropov YP, *Effect of Contact Deformations on the Adhesion of Particles*. Journal of Colloid and Interface Science, 1975(53): p. 314-326.
47. Kresse, G. and J. Hafner, *Ab initio molecular dynamics for liquid metals*. Physical Review B, 1993. **47**(1): p. 558.
48. Kresse, G. and J. Furthmüller, *Efficient iterative schemes for ab initio total-energy calculations using a plane-wave basis set*. Physical Review B, 1996. **54**(16): p. 11169.
49. Giustino, F., *Materials modelling using density functional theory: properties and predictions*2014: Oxford University Press.
50. Perdew, J.P., K. Burke, and M. Ernzerhof, *Generalized gradient approximation made simple*. Physical review letters, 1996. **77**(18): p. 3865.
51. Ruston, W., et al., *The solid reaction products of the catalytic decomposition of carbon monoxide on iron at 550 C*. Carbon, 1969. **7**(1): p. 47IN1551-50IN2057.
52. Monkhorst, H.J. and J.D. Pack, *Special points for Brillouin-zone integrations*. Physical Review B, 1976. **13**(12): p. 5188.
53. Yu, R., J. Zhu, and H. Ye, *Calculations of single-crystal elastic constants made simple*. Computer physics communications, 2010. **181**(3): p. 671-675.
54. Hill, R., *The elastic behaviour of a crystalline aggregate*. Proceedings of the Physical Society. Section A, 1952. **65**(5): p. 349.
55. Chung, R., et al., *Abnormal erosion–slurry velocity relationship of high chromium cast iron with high carbon concentrations*. Wear, 2011. **271**(9): p. 1454-1461.
56. Zhang, T. and D. Li, *Improvement in the corrosion-erosion resistance of 304 stainless steel with alloyed yttrium*. Journal of Materials Science, 2001. **36**(14): p. 3479-3486.

57. Hua, G. and D. Li, *Generic relation between the electron work function and Young's modulus of metals*. Applied Physics Letters, 2011. **99**(4): p. 041907.
58. Lu, H., G. Hua, and D. Li, *Dependence of the mechanical behavior of alloys on their electron work function—An alternative parameter for materials design*. Applied Physics Letters, 2013. **103**(26): p. 261902.
59. Pugh, S., *XCII. Relations between the elastic moduli and the plastic properties of polycrystalline pure metals*. The London, Edinburgh, and Dublin Philosophical Magazine and Journal of Science, 1954. **45**(367): p. 823-843.
60. Chen, X.-Q., et al., *Modeling hardness of polycrystalline materials and bulk metallic glasses*. Intermetallics, 2011. **19**(9): p. 1275-1281.
61. Fang, C., M. Van Huis, and H. Zandbergen, *Structural, electronic, and magnetic properties of iron carbide Fe₇C₃ phases from first-principles theory*. Physical Review B, 2009. **80**(22): p. 224108.
62. Music, D., et al., *Electronic structure and mechanical properties of Cr₇C₃*. Physics Letters A, 2004. **326**(5): p. 473-476.
63. Kittel, C., *Introduction to solid state*. Vol. 162. 1966: John Wiley & Sons.
64. Bader, R.F., *Atoms in molecules: a quantum theory, vol 22, International series of monographs on chemistry*, 1990, Oxford Science, Oxford.
65. Schwarz, K., *Band structure and chemical bonding in transition metal carbides and nitrides*. Critical Reviews in Solid State and Material Sciences, 1987. **13**(3): p. 211-257.
66. Zhang, R., et al., *Thermodynamic stability and unusual strength of ultra-incompressible rhenium nitrides*. Physical Review B, 2011. **83**(6): p. 060101.